Insights of biomass gasification combined with CO_2 absorption enhanced reforming in an 8 MW_{th} dual fluidized bed

Dali Kong [a], Shuai Wang [a,*], Kun Luo [a,b,*], Qilong Xu [a], Jianren Fan [a,b]

[a] *State Key Laboratory of Clean Energy Utilization, Zhejiang University, Hangzhou 310027, China*
[b] *Shanghai Institute for Advanced Study of Zhejiang University, Shanghai 200120, China*

ARTICLE INFO

ABSTRACT

Biomass gasification combined with CO_2 absorption enhanced reforming (AER) emerges as a clean and efficient technology for H_2 enrichment and CO_2 removal, yet an in-depth understanding of in-furnace phenomena and fundamental physics is still lacking. In this work, the AER gasification in an industrial-scale DFB reactor is numerically studied by integrating the multi-phase particle-in-cell (MP-PIC) framework with complex reaction kinetics regarding gasification, carbonation, and calcination. After model validations, the effects of several key operating parameters on the AER gasification performance are studied. As compared with conventional gasification, AER gasification promotes H_2 concentration by 15.3% but reduces CO_2 concentration by 55.8%, leading to syngas quality improvement. Moreover, AER gasification performance in the DFB reactor can be improved by: (i) increasing gasification temperature; (ii) increasing steam-to-biomass ratio; (iii) adjusting bed material and (iv) decreasing particle size. The present work provides a cost-effective tool to study the physical-thermal-chemical behaviors of AER gasification in industrial-scale DFB reactors.

1. Introduction

Biomass is an environmentally friendly resource with net zero carbon emissions [1-4]. In the life cycle of biomass material, only carbon that has been fixed through photosynthesis in the natural carbon cycle will be released. Therefore, the utilization of biomass will not lead to the exacerbation of climate change such as the greenhouse effect. However, the direct burning of biomass emits a large amount of gas and solid pollutants, which deteriorates the natural environment and human health [5]. Biomass gasification is a feasible technology to circumvent these issues. Specifically, biomass gasification refers to the thermo-chemical conversion of carbonaceous substances in biomass material into syngas mainly consisting of H_2 and CO using gasification agents (such as air, pure oxygen or steam, or mixtures of such components) [6,7] at a temperature of 500 to 1400 °C. Syngas can be used for power generation in gas engines, or high-value liquid fuels production in chemical reactors. Thus, biomass gasification has been increasingly investigated and applied both in academic and engineering communities. Currently, a major challenge in biomass gasification is the high content of CO_2 in the produced syngas, which reduces the calorific value and usable value of syngas. One feasible solution is to use CO_2 absorbent

to remove CO_2 generated in the gasification process and increase the combustible gas (mainly H_2) concentration in the syngas [8-10]. This process is termed absorption-enhanced reforming (AER) gasification. Calcium oxide (CaO) is commonly employed as a CO_2 absorbent and has received increasing attention due to its low costs and easy availability [11,12]. During the AER gasification process, the generated CO_2 will be absorbed by CaO, thereby changing the equilibrium composition of the syngas and promoting hydrogen production.

The dual fluidized bed (DFB) reactor, as a hetero-thermal gasification system, is naturally suitable for the AER gasification process. The traditional self-thermal gasification reactors (usually a single bubbling fluidized bed (BFB)) need to burn part of the biomass to provide the necessary heat for the gasification process and use air or pure oxygen as the gasification agents. The use of air as a gasification agent dilutes the syngas with nitrogen, and the separation of oxygen from air incurs high costs. In contrast, for the DFB reactor, a BFB serves as the gasifier while a circulating fluidized bed (CFB) serves as the combustor. The required heat for the gasification process is produced by the combustor and transferred into the gasifier via heat carriers. Therefore, the DFB systems generally use steam as the gasification agent, which prevents the produced syngas from being diluted by nitrogen and the high costs of using
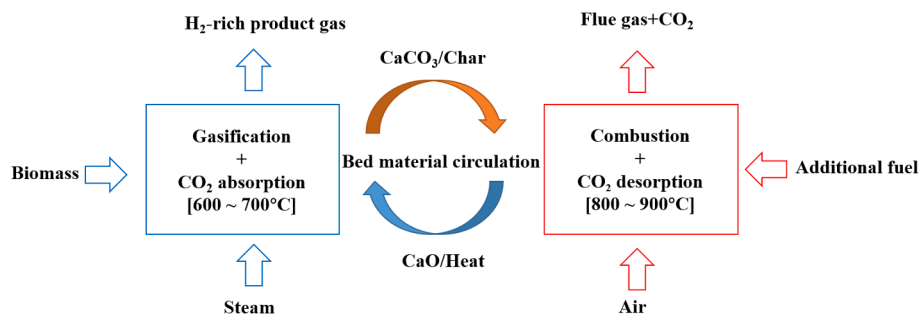
Fig. 1. The schematic of the AER gasification process in the DFB reactor.

pure oxygen as the gasification agent. In the AER gasification process in a DFB system, the bed material is mainly composed of CaO. In addition to its function as a heat carrier, CaO/CaCO₃ also acts as a CO₂ carrier and selectively transfers CO₂ from the gasifier to the combustor. As the bed material is circulated between these two reactors, carbonation and calcination reactions alternatively take place as follows [13]:

$$CaO \ + \ CO_2 \rightleftarrows CaCO_3 \tag{1}$$

As shown in Fig. 1, during the AER gasification, CaO and biomass are converted in the gasifier at 600 ~ 700 °C. By adsorbing CO₂, the parallel reforming/gasification reactions are driven in the direction that favors H₂ production. The gas products have low CO₂ concentration and high H₂ concentration accordingly. The carbonated bed material (CaCO₃) is regenerated by an endothermic calcination reaction in the combustor at 800 ~ 900 °C. The heat for the regeneration process comes from the combustion of unreacted char and additional supplemental fuel.

In recent years, plenty of efforts by experiments and simulations have been made in studying the AER gasification process in fluidized bed reactors [8,14,15]. However, the experimental method shows the intrinsic drawbacks in (i) the difficulty of obtaining the in-furnace phenomena from the micro-scale to the macro-scale; (ii) time-consuming and high-cost features due to the numerous trials and errors. In contrast, numerical simulation provides a cost-effective way to investigate the AER gasification process in fluidized bed reactors. To date, multi-scale numerical approaches for simulating dense gas–solid flow in particulate systems have been developed, which can be typically classified as the Eulerian-Eulerian (E-E) and Eulerian-Lagrangian (E-L) methods. In the E-E method, the gas and particle phases are regarded as a continuum and solved under the Eulerian framework. This method can predict the macroscopic properties of dense gas–solid flow systems at high computational efficiency [16]. However, the E-E method cannot resolve discrete features of the particle phase (e.g., rotation, shrinkage, size distribution). In a fluidized bed, the fundamental physics behind the macro-scale phenomena are commonly interpreted with the aid of micro-scale properties [17]. The E-E method is incapable of obtaining such information. In contrast, the E-L method can overcome the above drawback, as it treats the particle as a discrete phase and solves particle motions by Newton's second law. Computational fluid dynamics - discrete element method (CFD-DEM) and multi-phase particle-in-cell (MP-PIC) are two of the most representative approaches under the E-L framework. Specifically, the former fully resolves inter-particle collisions by tiny time-step and thus can obtain detailed microscopic information of the particle phase [3,18]. Therefore, the CFD-DEM approach has high solution accuracy but extremely low computational efficiency. The MP-PIC approach packages several real particles with the same properties (e.g., size, velocity, specie) into a parcel, and simplifies particle collisions by introducing a solid stress model. By these two strategies, this approach balances numerical accuracy and computational efficiency. So far, the MP-PIC approach has been extensively utilized to investigate biomass gasification in fluidized bed reactors. For example, Zhou et al. [19] used the MP-PIC method to numerically study biomass gasification in a bubbling fluidized bed and discussed the effect of the

particle size distribution (PSD) on gasification performance. They found that increasing the PSD width increased the total gas production, the concentration of combustible gas, and carbon conversion efficiency. Furthermore, larger PSD widths lead to larger mole fractions of combustible gas in the axial distribution. Thapa et al. [20] developed a 3D MP-PIC model to study the cold flow in a lab-scale circulating fluidized bed (CFB). They further extended the developed model for biomass gasification under high temperatures and figured out the optimal bed material circulation rate. At high temperatures and reaction conditions, for a given air supply rate, the bed material circulation rate decreased with the decrease of the bed material inventory across the CFB. Wan et al. [21] studied particle-scale thermochemical properties in a 1 MW_th pilot-scale DFB reactor using the MP-PIC method. They pointed out that the size-induced and density-induced particle segregation led to the preferential distribution of biomass particles near the bed surface. The particle segregation inhibited the mixing of biomass and bed material particles, deteriorating the gasification performance. The maximum temperature of biomass pellets occurred near the bed surface, and the wider PSD of bed material particles exacerbated the segregation of biomass particles. Kraft et al. [22] developed a cold-state flow model for an industrial-scale dual fluidized bed system based on the MP-PIC method. The effects of different drag models (EMMS, Ganser, Turton-Levenspiel, and Wen-Yu/Ergun) on parameters such as pressure, particle distribution, and bed material circulation rate were studied and compared with experimental data. The results showed that the Ganser drag model has the best performance in predicting bed material circulation rate.

The above studies provide meaningful information on micro-scale particle behaviors and macro-scale reactor performance regarding biomass gasification in pilot-scale fluidized bed reactors. Nevertheless, the mesoscale bubble behaviors in the reactor that bridge the micro-scale and macro-scale information have been seldom investigated for further understanding of the fundamental physics behind the in-furnace phenomena. Moreover, in the AER gasification process, the lower gasification temperature, the CO₂ removal, and its influence on the related parallel reactions greatly affect the hydrodynamics and thermochemical properties in the reactor, which is very different from the conventional biomass gasification process. To the best of our knowledge, numerical simulation of the AER gasification process in industrial-scale fluidized bed reactors has not been reported in the open literature.

To fulfill the knowledge gap, this work numerically investigates the AER gasification process in an 8 MW_th DFB reactor by integrating the MP-PIC framework with complex reaction kinetics regarding gasification, carbonation, and calcination. The AER gasification performance will be demonstrated and explained by comparing it with conventional gasification, with a focus on physical analysis and thermal analysis. The effect of critical operating parameters (e.g., gasification temperature, steam-to-biomass (S/B) ratio, and particle size distribution) on the gasification performance and bubble behaviors is illuminated. The article is structured as follows: section 2 gives the methodology including the thermophysical model and chemical reaction model. Section 3 gives the numerical settings and model validation. Section 4.1

demonstrates the superior performance of the AER gasification, followed by the underlying mechanism illustration in section 4.2. Section 4.3 shows the effect of critical operating parameters on the AER gasification in the DFB reactor. Section 5 gives the conclusion.

2. Methodology

In the MP-PIC approach, the solution of the transport equation of a particle distribution function (PDF) is used to denote particle dynamics while Navier-Stokes equations are adopted to describe gas motions. A shrink core model is used to describe the variation in particle diameter caused by heterogeneous reactions. The mathematical model is detailed below.

2.1. Thermodynamic model

For the gas phase, the conservation equations involving mass, momentum, energy, and species are formulated as [23,24]:

$$\frac{\partial(\theta_g \rho_g)}{\partial t} + \nabla \cdot (\theta_g \rho_g \boldsymbol{u}_g) = \delta \dot{m}_s \tag{2}$$

$$\frac{\partial(\theta_g \rho_g \boldsymbol{u}_g)}{\partial t} + \nabla \cdot (\theta_g \rho_g \boldsymbol{u}_g \boldsymbol{u}_g) = -\nabla p_g + \rho_g \theta_g \boldsymbol{g} + \nabla \cdot (\theta_g \boldsymbol{\tau}_g) + \boldsymbol{F}_{gs} \tag{3}$$

$$\frac{\partial(\theta_g \rho_g h_g)}{\partial t} + \nabla \cdot (\theta_g \rho_g \boldsymbol{u}_g h_g) = \theta_g \left(\frac{\partial p_g}{\partial t} + \boldsymbol{u}_g \cdot \nabla p_g \right) - \nabla \cdot (\theta_g q) + \dot{Q}_D + S_{gs} + S_{gw} - \Delta H_{rg} \tag{4}$$

$$\frac{\partial(\theta_g \rho_g Y_{g,k})}{\partial t} + \nabla \cdot (\theta_g \rho_g \boldsymbol{u}_g Y_{g,k}) = \nabla \cdot (\theta_g \rho_g D_{g,k} \nabla Y_{g,k}) + \delta \dot{m}_{k,react} \tag{5}$$

where ρ_g is the density; $\boldsymbol{u}_g$ is the velocity vector; p_g is the pressure; θ_g is the volume fraction; $\boldsymbol{g}$ is the gravitational acceleration. $\boldsymbol{F}_{gs}$ is the interphase momentum exchange term. $\delta \dot{m}_s$ is the source term that links the reaction of the discrete phase and continuous phase. h_g and $Y_{g,k}$ are the enthalpies of the mixture of gas and the mass fraction of kth gas species, respectively. $\delta \dot{m}_{k,react}$ is the consumption or production of kth gas species. $D_{g,k}$ is the mass diffusion coefficient. q is the heat flux. S_{gs} and S_{gw} are the gas-particle and gas-wall heat transfer. h_s is the gas enthalpy and $\dot{Q}_D$ is the gas enthalpy diffusion. The mass and energy conservation equations based on each parcel are given by:

$$\frac{dm_s}{dt} = \sum_{i=1}^{N} \frac{dm_{s,i}}{dt} \tag{6}$$

$$m_s C_V \frac{dT_s}{dt} = Q_{sg} + Q_{radi} - \Delta H_{rs} \tag{7}$$

where Q_{sg} and Q_{radi} represent the convective and radiative heat transfer flux, respectively. ΔH_{rs} is the heat flux from chemical reactions. The detailed calculations about the particle kinematics are summarized in Appendix A of the Supporting Information.

2.2. Chemical reaction model

After entering the gasifier, the moisture in the biomass particles is first released at high temperatures, followed by the volatiles. The drying process is characterized as follows:

$$\text{Moisture in Biomass} \rightarrow H_2O \ (g) \tag{8}$$

The drying kinetics is described with an equation of the Arrhenius type [25]:

Table 1
Chemical reaction and reaction rates [26,34].

Chemical reaction equation	Chemical reaction rate
R1: $C + O_2 \rightarrow CO_2$	$r_1 = 4.34 \times 10^7 m_c T_p \exp(-13590/T_p)[O_2]$
R2: $C + H_2O \leftrightarrow CO + H_2$	$r_{2f} = 6.36 m_c T_p \exp(-22645/T_p)[H_2O]$
	$r_{2r} = 5.218 \times 10^{-4} m_c T_p^2 \exp(-6319/T_p - 17.29)[H_2][CO]$
R3: $C + CO_2 \leftrightarrow 2CO$	$r_{3f} = 6.36 m_c T_p \exp(-22645/T_p)[CO_2]$
	$r_{3r} = 5.218 \times 10^{-4} m_c T_p^2 \exp(-2363/T_p - 20.92)[CO]^2$
R4: $C + 2H_2 \leftrightarrow CH_4$	$r_{4f} = 6.838 \times 10^{-3} m_c T_p \exp(-8078/T_p - 7.087)[H_2]$
	$r_{4r} = 0.755 m_c T_p^{0.5} \exp(-13578/T_p - 0.372)[CH_4]^{0.5}$
R5: $CO + 0.5O_2 \rightarrow CO_2$	$r_5 = 1.3 \times 10^{11} \exp(-15155/T_g)[CO][O_2]^{0.5}[H_2O]^{0.5}$
R6: $H_2 + 0.5O_2 \rightarrow H_2O$	$r_6 = 2.2 \times 10^9 \exp(-13110/T_g)[H_2][O_2]$
R7: $CH_4 + 2O_2 \rightarrow CO_2 + 2H_2O$	$r_7 = 5.01 \times 10^{11} \exp(-24117/T_g)[CH_4]^{0.7}[O_2]^{0.8}$
R8: $CH_4 + H_2O \rightarrow CO + 3H_2$	$r_8 = 3 \times 10^5 \exp(-15042/T_g)[CH_4][H_2O]$
R9: $CO + H_2O \rightarrow CO_2 + H_2$	$r_9 = 7.68 \times 10^{10} \exp(-36640/T_g)[CO]^{0.5}[H_2O]$
R10: $C_{16}H_{34} + 24.5O_2 \rightarrow 16CO_2 + 17H_2O$	$r_{10} = 3.8 \times 10^{11} \exp(-1.255 \times 10^8 / RT_g)[C_{16}H_{34}]^{0.25}[O_2]^{1.5}$

$$r_{drying} = 5.13 \times 10^{10} \exp\left(-\frac{10585}{T_p}\right)[\text{Moisture}] \tag{9}$$

where [Moisture] is the mass of moisture in the biomass particle.

The pyrolysis process is described as:

$$\text{Biomass} \rightarrow \alpha_1 CO + \alpha_2 CO_2 + \alpha_3 CH_4 + \alpha_4 H_2 + \alpha_5 \text{Char} + \alpha_6 \text{ash} \tag{10}$$
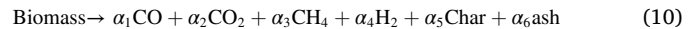
where α_i is determined according to the proximate and ultimate analysis of the biomass. Tar is hard to exist at high temperatures, and thus the hydrocarbon is represented by methane. To simplify the calculation, the elements such as N, S, and Cl are neglected due to their minor amounts. The above assumptions have been widely applied in previous studies [26–28]. The rate of the pyrolysis process is calculated by the single-step global reaction mechanism [29]:

$$r_{pyrolysis} = 1.49 \times 10^5 \exp\left(-\frac{1340}{T_p}\right)[\text{Volatile}] \tag{11}$$

where [Volatile] is the mass of volatile in the biomass particle.

CaO acts as both CO_2 sorbent and tar reforming catalyst in the AER gasification process [12]. Removing CO_2 from the gasification process as soon as it is formed changes the equilibrium composition of the produced gas and promotes the production of gas rich in hydrogen [11]. Similarly, the catalytic reforming of tar not only reduces the tar amount in the product gas but also enhances the total gas and hydrogen yields [30,31]. Udomsirichakorn et al. [32] studied the AER process in a lab-scale BFB reactor, aimed primarily at studying the tar reforming effect of in-bed CaO, and presented an in-depth analysis of the effect of CaO on tar yield. The results showed that compared to a bed of sand alone, a 20% higher H_2 concentration, an almost double H_2 yield, and a 67% reduction in tar content were obtained when a bed of CaO was used at the temperature of 650 °C and steam-to-biomass ratio of 3.41. Moreover, shifting the tar species from larger to fewer ring structures as a result of in-bed CaO could reduce tar dew point by 11 °C and tar carcinogenic potential by almost 60%. Koppatz et al. [13] experimentally studied the AER process in an industrial-scale DFB reactor, the results showed that during the steady state period, the tar accounted for 5.77 vol-%dry in the gas products at an average gasification temperature of 675 °C, while C_2H_6 accounts for 0.98 vol-%dry, C_2H_4 accounts for 2.42 vol-%dry, C_3H_8 accounts for 2.37 vol-%dry, and the proportion of each C_2–C_3 hydrocarbon component is lower than 3%. Based on the above evidence, the tar content is neglected in the present work, which is reasonable to some
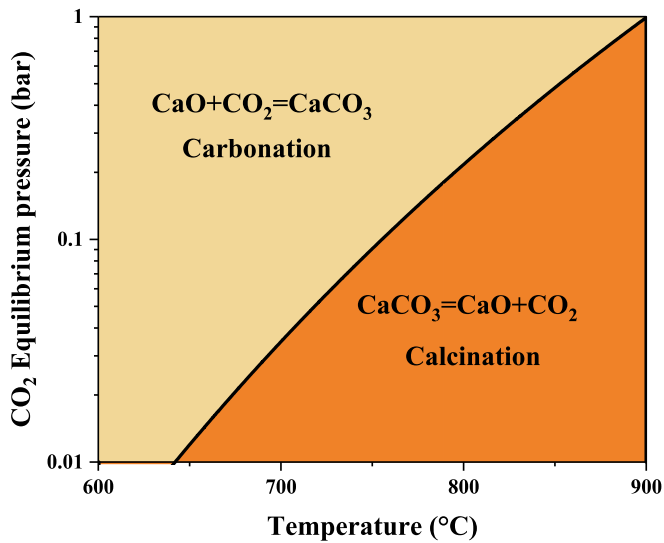
Fig. 2. The equilibrium diagram of the partial pressure of CO_2 regarding temperature [35].

extent.

In the gasifier, the gases and char produced by the pyrolysis process undergo a variety of homogeneous and heterogeneous reactions. In the combustor, a portion of the gas products and the additional fuel are burned to heat the bed material particles. The additional fuel is rapeseed methyl ester (RME), modeled as n-Hexadecane ($C_{16}H_{34}$), which is fed into the combustor as droplets. The reactions involved are drying and n-Hexadecane oxidation [33]. The relevant reactions as well as reaction rates are listed in Table 1.

In the AER gasification process, the carbonation and calcination reactions of CaO are described as:

$$CaO + CO_2 \rightleftarrows CaCO_3 \tag{12}$$
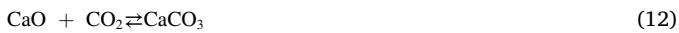
The carbonation and calcination reactions in the reactor are driven by the discrepancy between the partial pressure of CO_2 (P_{CO2}) and the equilibrium partial pressure of CO_2 ($P_{CO2, eq}$). $P_{CO2, eq}$ is mainly determined by experiments. Baker [35] proposed a widely used expression of $P_{CO2, eq}$ as below, with the equilibrium diagram shown in Fig. 2.

$$\log_{10}P_{co_2,eq} = 7.079 - \frac{8308}{T_g} \tag{13}$$

The P_{CO2} higher than $P_{CO2, eq}$ results in carbonation, whereas P_{CO2} lower than $P_{CO2, eq}$ leads to calcination. These thermodynamic properties determine the temperature range of the AER gasification process. The carbonation reaction requires a temperature ranging from 600 °C to 700 °C, based on a typical CO_2 mole concentration of 10 ~ 20% in the gas products [13].

The reaction rate of carbonation is calculated using the correlation proposed by Sun et al. [36]:

$$R_{carb} = 56K_s(1 - X_{carb})(P_{co_2} - P_{co_2,eq})^n S \tag{14}$$

where X_{carb} is the conversion of CaO, and n is the reaction order:

$$n = 1, \ P_{co_2} - P_{co_2,eq} \leqslant 10 \text{ kPa} \tag{15}$$

$$n = 0, \ P_{co_2} - P_{co_2,eq} > 10 \text{ kPa} \tag{16}$$

where S is the specific surface area of the CaO particle. K_s is the reaction rate coefficient, given by:

$$K_s = 1.67 \times 10^{-4}\exp(\frac{-E}{RT}), \ E = 29 \pm 4 \text{ KJ/mol}, \ P_{co_2} - P_{co_2,eq} \leqslant 10 \text{ kPa} \tag{17}$$

$$K_s = 1.04 \times 10^{-4}\exp(\frac{-E}{RT}), \ E = 24 \pm 6 \text{ KJ/mol}, \ P_{co_2} - P_{co_2,eq} > 10 \text{ kPa} \tag{18}$$

The reaction rate of calcination reaction is described as [37]:

$$R_{calc} = 56K_{calc}(1 - X_{calc})^{2/3}(1 - \frac{P_{co_2}}{P_{co_2,eq}})^{1.86} \tag{19}$$

where X_{calc} is the conversion of $CaCO_3$, K_{calc} is the reaction rate

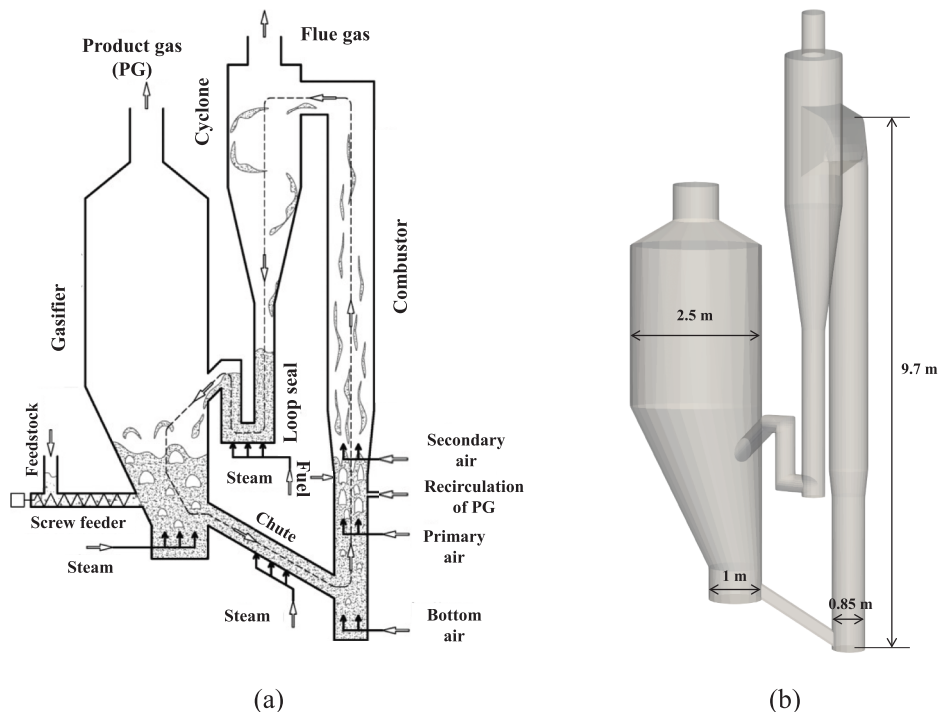(a)   (b)

Fig. 3. The investigated DFB reactor: (a) schematic diagram; (b) geometric diagram.

Table 2
Proximate analysis and ultimate analysis of biomass (wet basis).

Ultimate analysis (%)					Proximate analysis (%)				
C	H	O	N	S	M	A	V	FC	LHV (KJ/Nm^3)
48.40	6.09	45.3	0.2	0.01	33	1	56	10	18.18

Table 3
Operating temperatures in the two gasification conditions.

Reactor	Conventional gasification	AER gasification
Gasifier	850 °C	550 ~ 700 °C
Combustor	950 °C	850 °C

coefficient, given by:

$$K_{calc} = 5.61 \times 10^5 \exp(\frac{-150000}{RT}) \qquad (20)$$

3. Computational setups

3.1. Numerical settings

The investigated 8 MW$_{th}$ DFB reactor refers to a part of combined heat and power plant located in Austria. Fig. 3 depicts the geometry of the investigated DFB reactor [38]. Specifically, the whole system includes a gasifier and a combustor, which are connected by a cyclone separator, loop seal, and chute. Specifically, the gasifier operates in a bubbling fluidization state with steam as the fluidizing gas and gasification agent. Biomass particles are rapidly dried and pyrolyzed under high temperatures after entering the gasifier. The pyrolysis products undergo homogeneous and heterogeneous reactions in the gasifier. The gas products overflow from the exit of the gasifier. With air as the fluidizing gas, the combustor operates in a fast fluidization state. Bed material and incompletely reacted char particles enter the combustor through the chute. In the oxidizing atmosphere, char, additional fuel, and the recirculated dry gas products burn and release heat to heat the bed material. The flue gas and bed material are separated in the cyclone separator, the flue gas is discharged from the exit, and the bed material is transported to the gasifier through the loop seal. The heated bed material provides heat to support chemical reactions in the gasifier. Steam fluidization is used at the loop seal to prevent flue gas from entering the gasifier. The proximate analysis and ultimate analysis of biomass feedstock (*i.e.*, hardwood) are given in Table 2 [13,33]. The diameter of the lower and upper parts of the gasifier, the diameter of the combustor, and the height of the combustor are 1.0 m, 2.5 m, 0.85 m, and 9.7 m, respectively. To achieve a balance between numerical accuracy and computational load, the computational domain is divided into 215,280 grids based on the grid-independence test as shown in Appendix B of the Supporting Information.

In this work, the conventional gasification and AER gasification conditions of the DFB reactor are investigated. The operating temperatures in the two gasification conditions are shown in Table 3. Besides, the particle size distribution (PSD) follows the normal distribution:

$$f = \frac{1}{\sigma\sqrt{2\pi}}e^{-\frac{(d-d_a)^2}{2\sigma^2}} \qquad (21)$$

where d_a is the mean particle diameter, σ is the standard deviation.

The PSD of the biomass particles is 9 ~ 22 mm with a density of 800 kg/m^3. Under the conventional gasification condition, the bed material particle used is olivine with a density of 2800 kg/m^3 and PSD of 0.3 ~ 0.71 mm, which is consistent with the experimental measurement [39]. Under the AER gasification condition, the bed material particle used is calcined calcite, and its compositions are listed in Table 4 [40]. The PSD of calcined calcite is 0.5 ~ 1.3 mm, with a density of 2100 kg/m^3, which is consistent with the experimental measurement [15].

Initially, bed material particles are packed at the loop seal and the bottom of the gasifier and combustor with a total mass of 3000 kg. To monitor the gas product composition and the mass flux between the reactors, monitoring planes are set at the reactors outlet and the loop seal. The device is initially filled with nitrogen. The physical time of each case lasts 100 s. Table 5 lists the detailed operating parameters.

Specifically, four sets of gasification temperatures (*i.e.*, 550 °C, 600 °C, 650 °C, and 700 °C) and steam-to-biomass (S/B) ratios (*i.e.*, 0.1226, 0.1726, and 0.2226) are specified to investigate their effects on the AER gasification. Furthermore, four sets of PSDs are used to investigate the relationship between gas–solid hydrodynamics and gasification performance under the AER gasification condition. The detailed operating parameters are listed in Table 6.

The generation, coalescence, and breakage of bubbles take place in the gasifier. As a mesoscale structure, the behaviors of bubbles dominate the hydrodynamics in the reactor, significantly affecting the spatial distribution of particles and gases, and the resultant reactor performance. Therefore, it is of great significance to investigate bubble behaviors and illuminate their relationship with hydrodynamics and thermochemical behaviors. In this work, a novel bubble detection algorithm is developed, the implementation and verification of which are given in Appendix C of the Supporting Information.

Table 5
Operating parameters of the DFB reactor under the two gasification conditions.

Parameters	Conventional gasification	AER gasification
Gasifier		
Biomass feed rate (kg/s)	0.717	0.717
Biomass temperature (K)	298	298
Inlet steam flow rate (kg/s)	0.1238	0.1238
Steam temperature (K)	673	673
Combustor		
Bottom air flow rate (kg/s)	0.266	0.24
Bottom air temperature (K)	695	695
Primary air flow rate (kg/s)	0.75	0.67
Primary air temperature (K)	695	695
Secondary air flow rate (kg/s)	0.415	0.371
Secondary air temperature (K)	695	695
Gas products flow rate (kg/s)	0.0194	0.0174
Gas products temperature (K)	353	353
RME flow rate (kg/s)	0.0078	0.007
RME temperature (K)	353	353
Operating pressure (MPa)	1	1
Solid volume fraction at close pack (-)	0.58	
Particle normal-to-wall retention coefficient (-)	0.9	
Particle tangential-to-wall retention coefficient (-)	0.3	
Fraction coefficient (-)	0.3	
Time step (s)	2.0 × 10^{-5}	

Table 4
Composition of the calcined calcite.

Composition	CaO	CaCO$_3$	MgO	SiO$_2$	Fe$_2$O$_3$	Al$_2$O$_3$	Trace elements
Proportion (%)	71.25	22.75	0.7	2.77	0.6	1.4	0.53

Table 6
Operating parameters and values investigated in the present work.

Case	d_p (mm)	T_b (C)	S/B (-)
Base case	0.5 ~ 1.3	650	0.1726
Calcined limestone particle diameter	0.4 ~ 1.2	650	0.1726
	0.45 ~ 1.25	650	0.1726
	0.5 ~ 1.3	650	0.1726
	0.55 ~ 1.35	650	0.1726
Gasification temperature	0.5 ~ 1.3	550	0.1726
	0.5 ~ 1.3	600	0.1726
	0.5 ~ 1.3	650	0.1726
	0.5 ~ 1.3	700	0.1726
Steam-to-biomass ratio	0.5 ~ 1.3	650	0.1226
	0.5 ~ 1.3	650	0.1726
	0.5 ~ 1.3	650	0.2226
	0.5 ~ 1.3	650	0.2726

3.2. Model validation

3.2.1. Validation I: Biomass gasification in a CFB gasifier

The reactive model is first validated with biomass gasification in a CFB gasifier experimentally conducted by Garíca-Ibañez et al [41]. Fig. S5(a) in Appendix D of the Supporting Information presents the schematic of the CFB gasifier. Primary airflow is introduced from the bottom to fluidize the particles and acts as a gasifying agent. The secondary airflow is injected from a feeding port 2.15 m above the bottom to support reactions. The silica sand is adopted as the bed material with a mean diameter and density of 0.5 mm and 2600 kg/m³, respectively. The analysis and physical properties of biomass are listed in Table S1 in Appendix D of the Supporting Information. Fig. S5(b) shows the comparison between the simulation results and experimental data in terms of the mole fraction of the main gas components (*i.e.*, CO, CO₂, H₂, CH₄, hydrocarbon components, and N₂). It is noted that the predicted gas concentration agrees well with that obtained from experimental measurements. The slight discrepancies stem from the impractical implementation of the numerous elementary reactions during biomass gasification.

3.2.2. Validation II: Biomass gasification in a DFBG

An additional model validation towards biomass gasification is conducted in a pilot-scale DFB located at Woodland Biomass Research Center, Woodland, California [27]. The schematic diagram of the studied DFB is shown in Fig. S6(a) in Appendix D of the Supporting Information. The DFB consists of a BFB gasifier and a combustor reactor. At the initial stage, the bed material particles are packed at the bottom of the reactor with an initial height of 2500 mm. The steam is injected from the bottom of the gasifier to fluidize particles and acts as a gasifying agent. The propane is introduced into the combustor to maintain the temperature. The biomass particles are continuously fed into the gasifier. The analysis and physical properties of biomass are given in
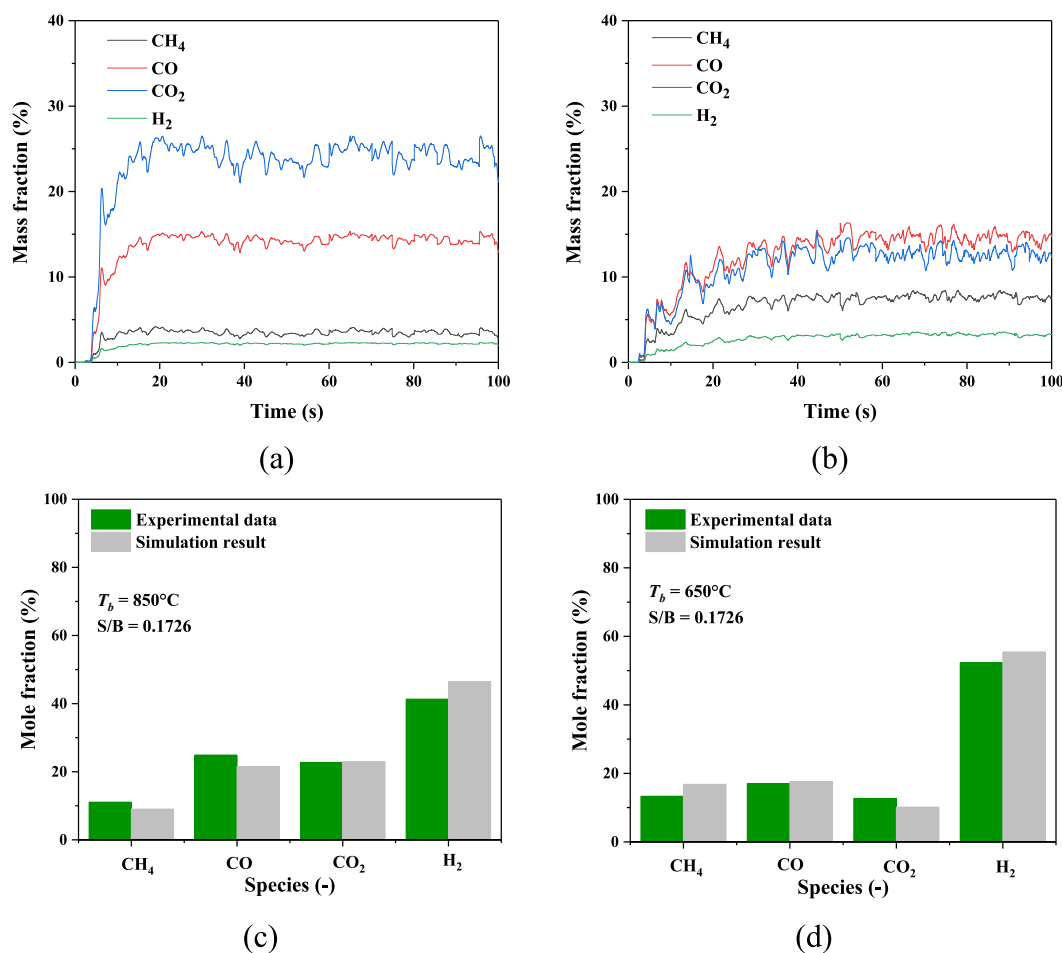

Fig. 4. Model validation regarding the gas products: (a) time-evolution of gas species concentration under the conventional gasification; (b) time-evolution of gas species concentration under the AER gasification; (c) time-averaged mole fractions under the conventional gasification; (d) time-averaged mole fractions under the AER gasification.
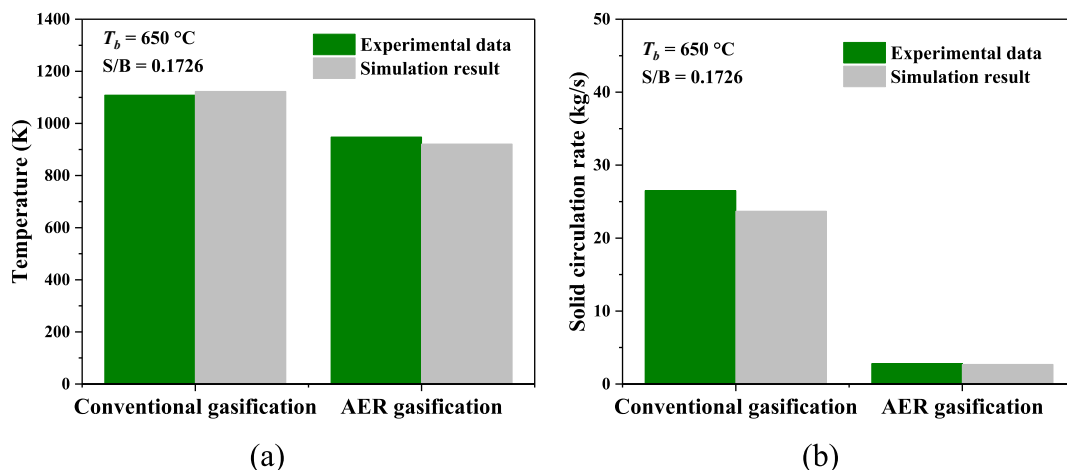
Fig. 5. Model validation regarding the gasification temperature and solid circulation rate of the two gasification conditions: (a) gasification temperature; (b) solid circulation rate.

Table S2 of the Supporting Information. As illustrated in Fig. S6(b), the predicted concentration of the product gas species agrees well with the experimental data. The slight discrepancy is attributed to the simplification of reaction kinetics. Therefore, the present MP-PIC model is reasonable to be employed to study biomass gasification in the DFB. Moreover, the numerical accuracy of the integrated model is not affected by operating conditions (e.g., the mass flow rate of solid fuels) as the equations or formulas governing gas–solid flow dynamics, heat transfer, and chemical reactions are unchanged. Therefore, the integrated model is reliable for the simulation of biomass gasification in the DFB under different operating conditions.

3.2.3. Validation III: Conventional and AER gasification in a 8 MW$_{th}$ DFB reactor

The model is further validated with the experimental work conducted by Koppatz et al. [13], in which gas–solid parameters and operating conditions are provided in section 3.1. Fig. 4(a, b) shows the concentration of gas products over time under conventional gasification

and the AER gasification conditions. After the initial start-up process, the concentrations of gas species fluctuate around fixed values after $t = 30$ s, indicating that the thermochemical behaviors in the reactor reach a dynamic equilibrium state. Therefore, the data after 30 s are employed for time averaging. As shown in Fig. 4(c, d), the simulated values agree well with experimental data [13] under the conventional gasification and AER gasification conditions. The discrepancy between the numerical results and experimental data comes from two aspects. First, there are hundreds of homogeneous and heterogeneous reactions in the conventional gasification and AER gasification processes, indicating the impractical implementation of such complex reactions in the model. Thus, the simplification of detailed chemical reactions into several global reactions inevitably introduces relative errors. Secondly, even for a specific global reaction, a set of reaction kinetics (e.g., pre-exponential factor and activation energy) exist according to the different literature [42–45]. Thus, the assignment of reaction kinetics referring to specific literature inevitably introduces relative errors [46]. Although the above-mentioned relative errors will be introduced during the simulation, the discrepancies between numerical results and experimental data are acceptable in the present work. Hence, the present model can be

used to reliably predict the thermochemical properties of the conventional gasification and the AER gasification process in DFB reactors.

Fig. 5 shows the comparison of experimental data [13] and simulation results of gasification temperature and solid circulation rate after reaching a steady state under the two gasification conditions. The gasification temperature refers to the average temperature in the gasifier. As shown in the figure, the simulated gasification temperature and solid circulation rate agree well with the experimental data, indicating that the developed model can reasonably predicate the hydrodynamics and thermochemical behaviors in the reactor.

4. Result and discussion

4.1. Performance comparison of two gasification conditions

Lower heating value (LHV) [28] and combustible gas (*i.e.*, H$_2$, CO, CH$_4$) concentration (CGC) [26], are adopted to evaluate the gasification performance, formulated as:

$$\text{LHV (MJ/Nm}^3) = (25.7 \times H_2\% + 30.3 \times CO\% + 85.4 \times CH_4\%) \times (4.2 / 1000) \tag{22}$$

$$\text{CGC (\%)} = \text{The volume summation of combustible gas in syngas/ Total volume of syngas (without H}_2\text{O)} \times 100\% \tag{23}$$

Compared with conventional gasification, AER gasification reduces the CO$_2$ concentration by 55.8% and improves the H$_2$ concentration by 15.3% (see Fig. 4). Under conventional gasification and AER gasification, the LHV of the gas products are 10.99 MJ/Nm^3 and 14.25 MJ/Nm^3, respectively, and the CGC is 77.02% and 89.84%, respectively, indicating that AER gasification significantly improves gasification performance. The gasification performance of the DFB reactor is highly determined by in-furnace flow dynamics and heat transfer, and thus it is essential to study the physical-thermal behaviors of gas–solid flow in the DFB reactor to unveil the performance superiority of the AER gasification.

4.2. Underlying mechanism of the higher performance of AER gasification

4.2.1. Physical analysis
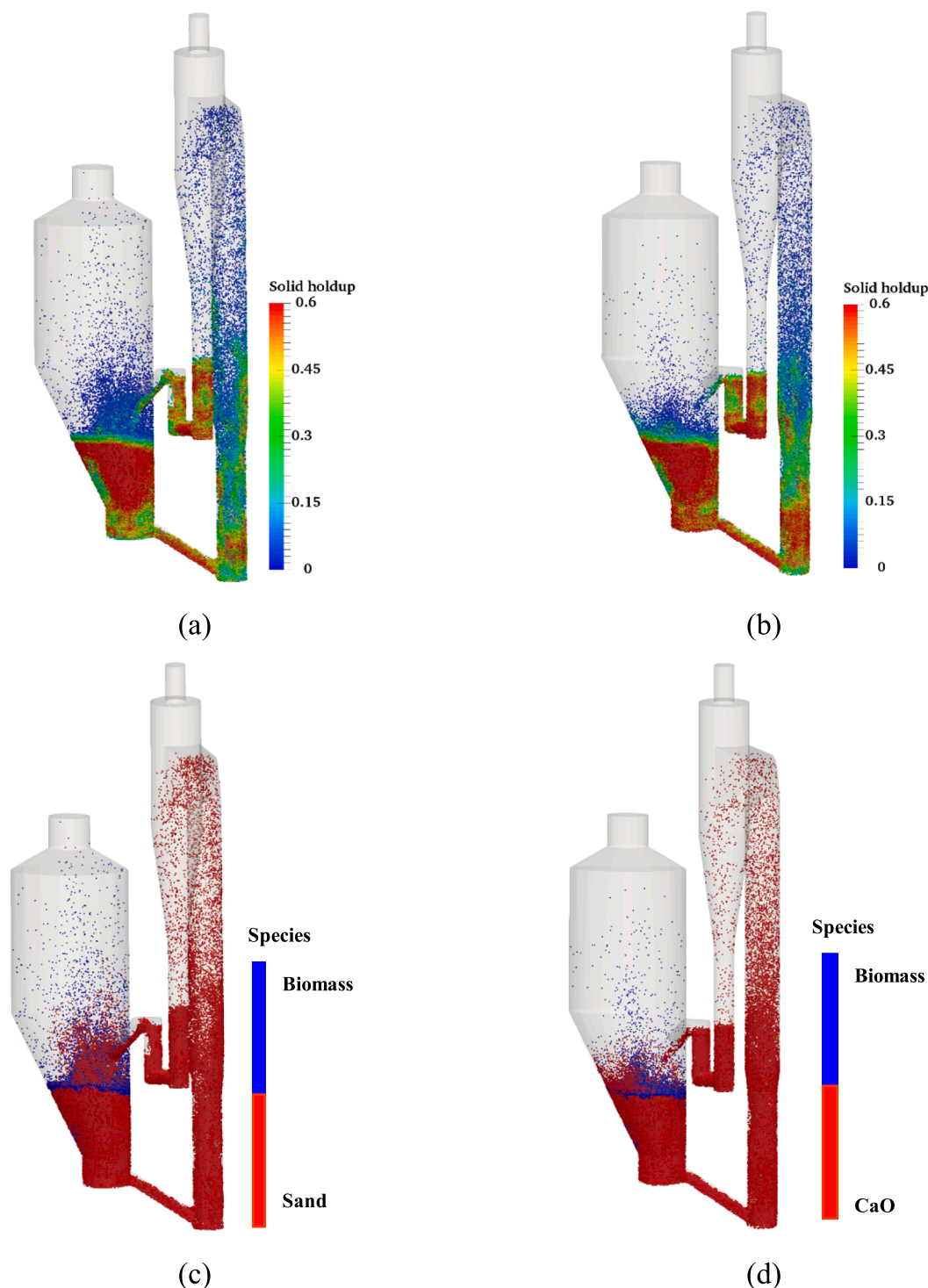Fig. 6 and Fig. 7 show the gas–solid flow patterns after the system

Fig. 6. Snapshots of solid holdup and particle species in the DFB reactor under conventional gasification condition (left column) and AER gasification condition (right column): (a, b) solid holdup; (c, d) solid species. (Note that the particle size is enlarged for better visualization).

reaches dynamic equilibrium under the convention gasification and AER gasification conditions. In the gasifier, the introduction of steam from the bottom leads to the formation of bubbles. As the bubbles rise, small-size bubbles merge into large-size bubbles, which dominate the gas–solid motions in the gasifier. At the bed surface, the bubbles break and cause large quantities of particles to be thrown into the freeboard region (Fig. 6(a, b)). Biomass particles tend to be distributed on the bed surface because of the density-induced and size-induced segregation while gasification proceeds (Fig. 6(c, d)). As compared with the AER

gasification condition, particles are distributed more dispersedly above the bed surface of the gasifier under the conventional gasification condition due to the higher temperature, which will be further discussed in the following sections. In the combustor, large vertical particle velocity can be observed. In addition, vigorous particle horizontal motions can also be observed due to the vigorous inter-particle and inter-phase interactions in the reactor. As compared with the AER gasification condition, the conventional gasification condition leads to more vigorous segregation due to the more significant bed expansion caused by higher
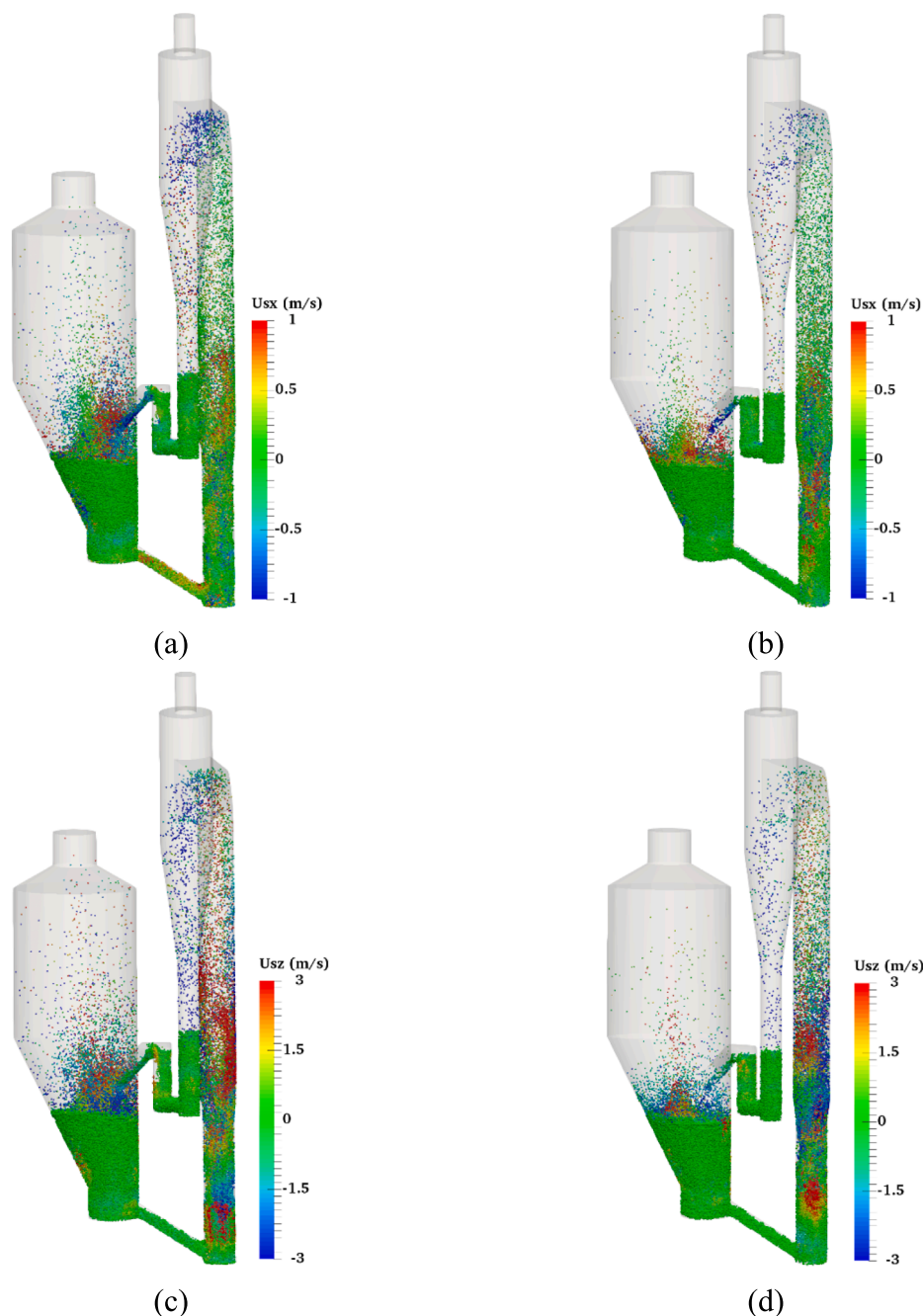
Fig. 7. Snapshots of horizontal particle velocity (Usx) and vertical particle velocity (Usz) in the DFB reactor under the conventional gasification condition (left column) and AER gasification condition (right column): (a, b) Usx; (c, d) Usz. (Note that the particle size is enlarged for better visualization).

Table 7
Particle mass flow rate under the two gasification conditions, $T_b = 650$ °C, S/B ratio = 0.1726.

Gasification type	Conventional gasification	AER gasification
Solid circulation rate (kg/s)	23.24	2.69

temperatures.

Table 7 shows the solid circulation rate between the reactors under the AER and the conventional gasification conditions. The particle mass flow rate under the conventional gasification condition is 23.24 kg/s, consistent with the typical value of the DFB reactor [33]. In contrast, the particle mass flow rate under the AER gasification condition is 2.69 kg/s,

which is one order of magnitude less than that under the conventional gasification condition. The lower particle mass flow rate ensures the steady operation of the gasifier at a lower operating temperature, which facilitates the carbonation reaction.

4.2.2. Thermal analysis

Fig. 8 and Fig. 9 show temperature distributions of the gas and particle phases under the conventional gasification and AER gasification conditions. In general, the gasifier where the endothermic gasification reactions occur has a lower temperature than the combustor where the exothermic oxidation reactions occur. In the gasifier, low-temperature biomass particles are distributed on the bed surface. The low-temperature bed material particles are transferred to the combustor from the gasifier through the chute. After undergoing the heating
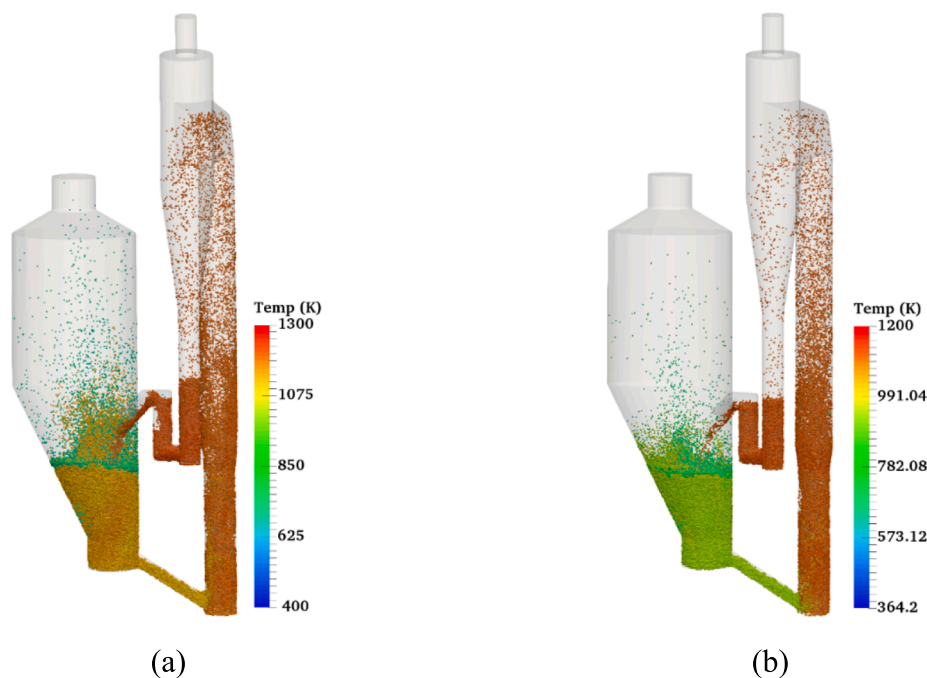
Fig. 8. Snapshots of particle temperature distribution under different gasification conditions: (a) conventional gasification condition; (b) AER gasification condition.
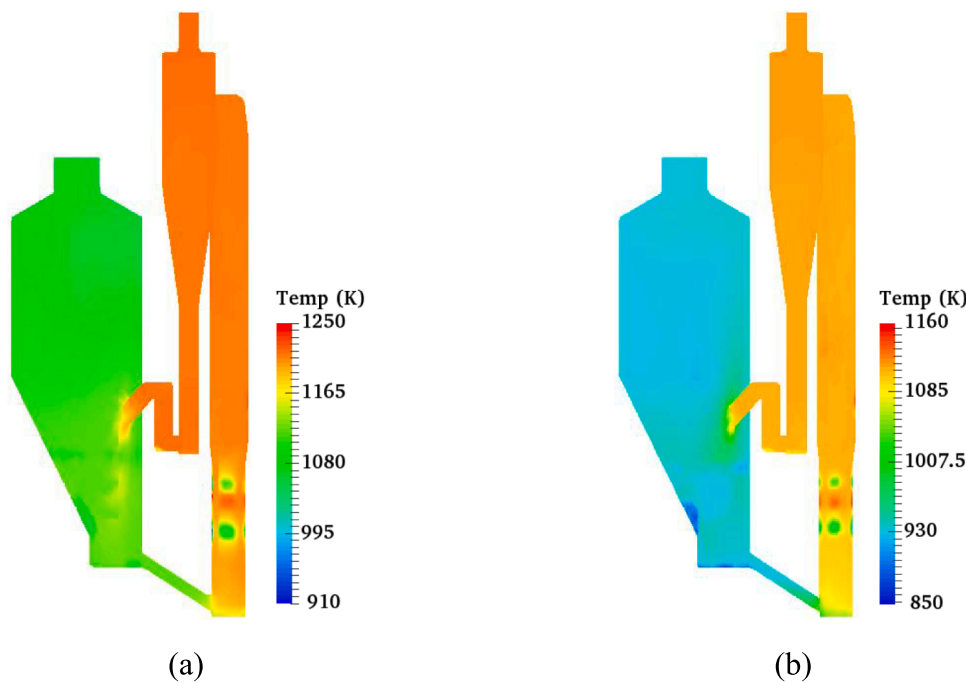

Fig. 9. Snapshots of gas temperature distribution under different gasification conditions: (a) conventional gasification condition; (b) AER gasification condition.

process, it enters the gasifier again via the cyclone separator. Thus, bed material acts as the heat carrier between the reactors to support the thermal status and continuous operation of the DFB reactor. Moreover, bed material under the AER gasification condition also acts as the CO_2 carrier. The combustion of solid fuels results in some obvious hot points in the lower part of the combustor. Under the conventional gasification condition, the higher solid circulation rate leads to higher-temperature particle flow in the dense phase region of the gasifier.

Fig. 10 gives the spatial profile of time-averaged gas temperature in the gasifier and combustor under the two gasification conditions. In the gasifier, under the effects of the high-temperature particles transported

from the combustor, the temperature of the gas phase first increases along with the bed height, and then gradually decreases due to the influence of the endothermic gasification reactions. Under the AER gasification condition, the larger temperature difference between the reactors leads to a more violent temperature variation in the gasifier. In the combustor, the introduction of low-temperature particles and gas agents results in a considerably low-temperature region in the lower part. Along with the bed height, the temperature gradually rises as the heat is released from the combustion of solid fuels, and the temperature remains stable in the region above 4 m. The temperature in the gasifier and combustor under the AER gasification condition respectively
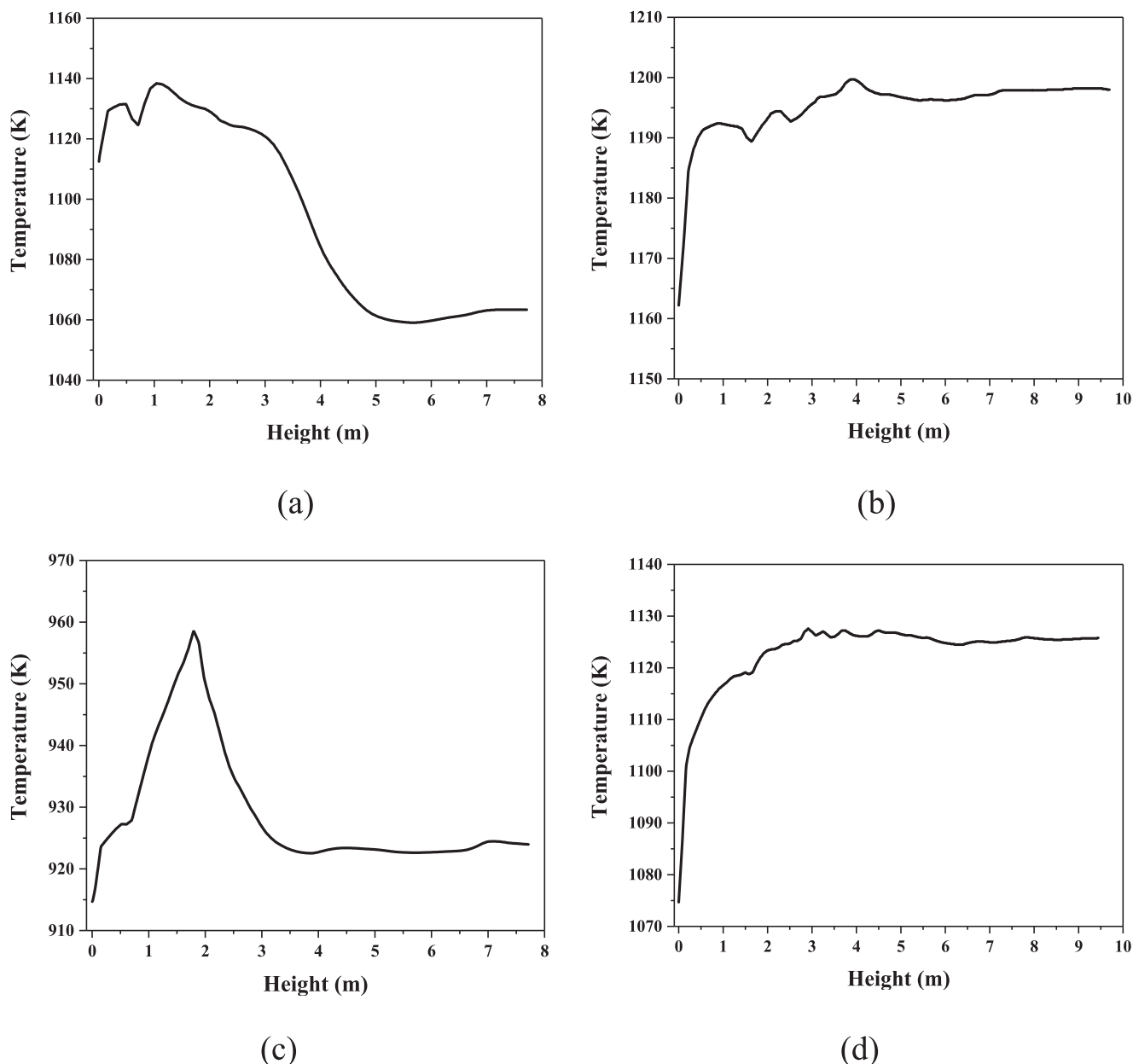
Fig. 10. Spatial profile of time-averaged gas temperature in the DFB reactor under the two gasification conditions: (a) gasifier under the conventional gasification condition; (b) combustor under the conventional gasification condition; (c) gasifier under the AER gasification condition; (d) combustor under the AER gasification condition.

decreases by about 200 K and 100 K than that under the conventional gasification condition, which is beneficial for the progress of the carbonation reaction and the improvement of the quality of the syngas.

Fig. 11 gives the variation of char mass in biomass particles with particle residence time in the gasifier of the AER gasification process. After entering the gasifier, the biomass particles undergo drying and pyrolysis, and then the residual char is involved in gasification, where the char mass continues to decline with the increase of particle residence time in the gasifier. It is noted that the char mass has an overall decreasing trend with the residence time of biomass particles in the gasifier.

4.3. Effect of critical operating parameters on the AER gasification

The above sections demonstrate the higher gasification performance in the DFB reactor under the AER condition. In this section, the effects of

critical operating parameters (e.g., gasification temperature, S/B ratio, and particle size) on the gasification performance under the AER gasification condition are investigated to figure out the optimal operating condition.

4.3.1. Gasification temperature

Fig. 12 gives the effects of the gasification temperature on the gasification performance under the AER gasification. The H_2 concentration in the gas product rises from 47.84% to 58.32%, and the CO_2 concentration decreases from 14.67% to 8.89%. High temperature strengthens carbonation reaction, leading to a decrease in CO_2 concentration and affecting the related parallel reactions (water–gas shift reaction (R2), methane steam reforming reaction (R8), etc.). The decrease in the CO and CH_4 concentrations confirmed this conclusion. Fig. 10(b) gives the effects of gasification temperature on the CGC and LHV. With the gasification temperature rising, the CGC rises from 85.33% to 91.11%. As
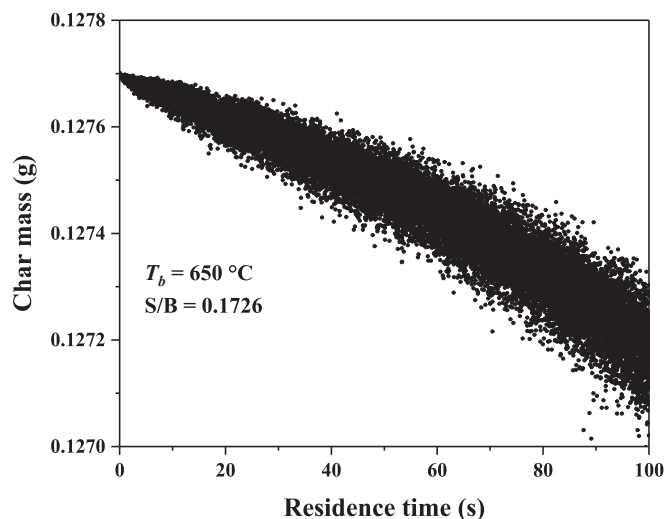
Fig. 11. Variation of char mass in biomass particles with particle residence time.

the gasification temperature increases from 550 °C to 650 °C, the LHV rises. When the gasification temperature exceeds 650 °C, the LHV decreases, which is attributed to the decrease in the CO and CH_4 concentrations with high calorific values in the gas products.

Fig. 13 gives the effect of gasification temperature on the bubble-to-emulsion phase volume (B/E) ratio in the gasifier and the solid circulation rate between the two reactors under the AER gasification condition. Specifically, the bubble phase is defined as a specific region in the gasifier with a voidage larger than 0.8, while the emulsion phase is defined as a specific region in the gasifier with a solid holdup less than 0.2. The bubble phase and emulsion phase are determined by the bubble detection algorithm developed in this work. It is noted the B/E ratio and the solid circulation rate increase with gasification temperature. Moreover, the two quantities are positively correlated. The gas volume expanding at high temperatures leads to larger bubble volumes and more intense gas–solid motions in the gasifier, and more particles are transferred to the combustor. Accordingly, the solid circulation rate between the two reactors increases, which maintains a stable temperature inside the gasifier and indicates the excellent temperature control performance of the DFB reactor.

The char conversion χ_{char} is calculated as:

$$\chi_{char} = \frac{\left| \frac{1}{n}\sum_{i=1}^{n} m_{char\ i,\ 100\ s} - \frac{1}{n_1}\sum_{i=1}^{n_1} m_{char\ i,\ 30\ s} \right|}{\frac{1}{n}\sum_{i=1}^{n} m_{char\ i,\ 100\ s}} \qquad (24)$$
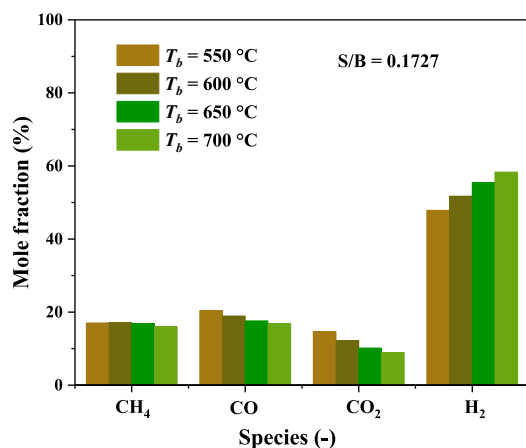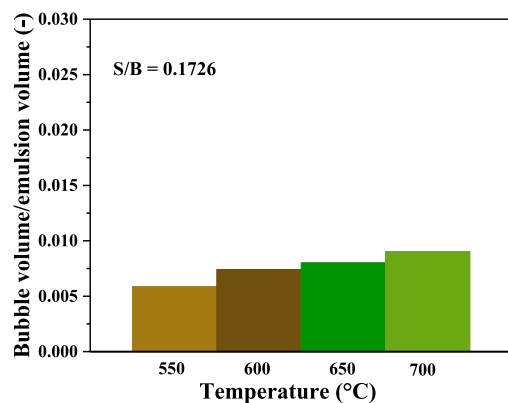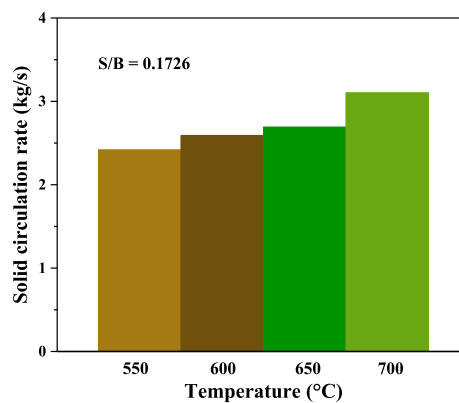

(a)
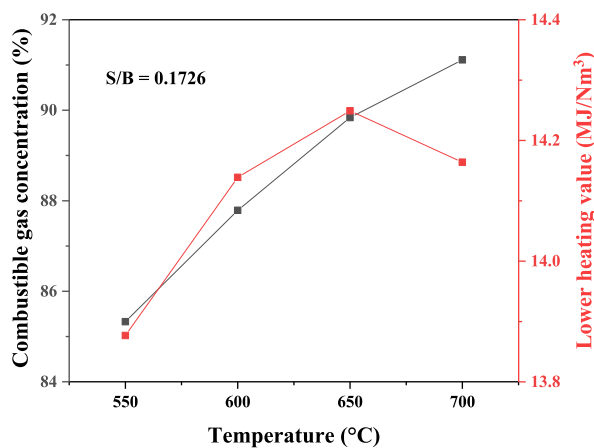
(b)

Fig. 12. The concentration of gas species (a) and CGC and LHV (b) under the AER gasification conditions as a function of gasification temperature.

(a)

(b)

Fig. 13. The B/E ratio in gasifier (a), and solid circulation rate between the two reactors (b) under the AER gasification condition as a function of gasification temperature.
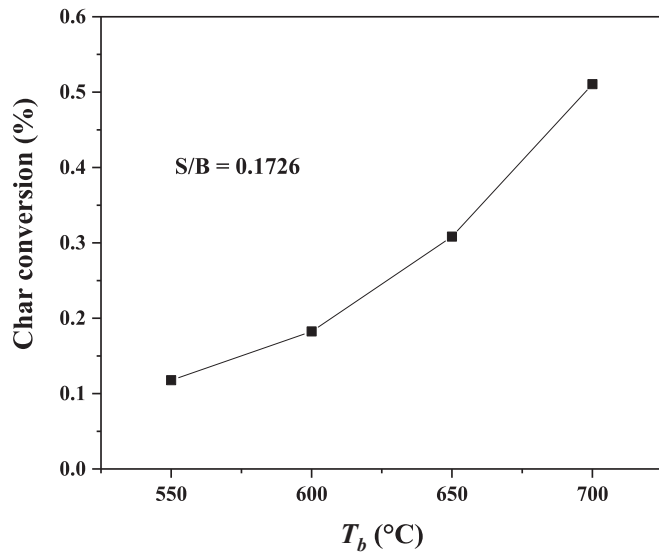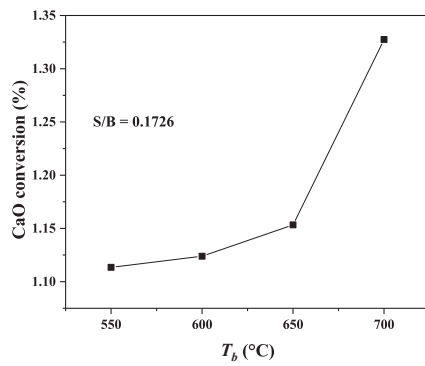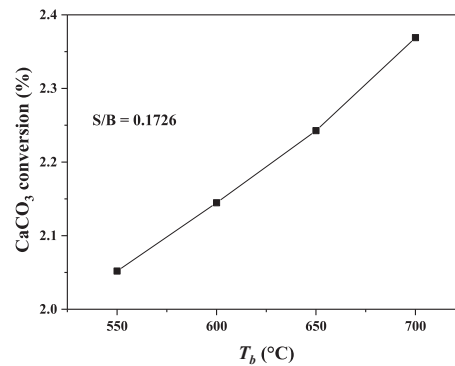
Fig. 14. Variation of the char conversion with gasification temperature.

where n and n_1 are the total number of biomass particles in the gasifier at $t = 100$ s and $t = 30$ s, respectively. $m_{\text{char } i, \, 100 \text{ s}}$ is the mass of char in biomass particle i at $t = 100$ s, and $m_{\text{char } i, \, 30 \text{ s}}$ is the mass of char in biomass particle i at $t = 30$ s.

Fig. 14 shows the variation of the char conversion under different gasification temperatures. It is noted that the char conversion increases with the increase in gasification temperature. A higher gasification temperature promotes the char gasification reactions (R2, R3). Moreover, the CO_2 absorption by CaO affects the progress of the related parallel reactions, changes the concentration of gas components in the reactor, and thus promotes char conversion.

Similarly, the CaO conversion in the gasifier and the $CaCO_3$ conversion in the combustor are respectively calculated as

$$\chi_{\text{CaO}} = \frac{\left| \frac{1}{q}\sum_{j=1}^{q} m_{\text{CaO } j, \, 100 \text{ s}} - \frac{1}{q_1}\sum_{j=1}^{q_1} m_{\text{CaO } j, \, 30 \text{ s}} \right|}{\frac{1}{q}\sum_{j=1}^{q} m_{\text{CaO } j, \, 100 \text{ s}}} \tag{25}$$

$$\chi_{\text{CaCO}_3} = \frac{\left| \frac{1}{m}\sum_{k=1}^{m} m_{\text{CaCO}_3 \, k, \, 100 \text{ s}} - \frac{1}{m_1}\sum_{k=1}^{m1} m_{\text{CaCO}_3 \, k, \, 30 \text{ s}} \right|}{\frac{1}{m}\sum_{k=1}^{m} m_{\text{CaCO}_3 \, k, \, 100 \text{ s}}} \tag{26}$$

where q and q_1 are the total number of calcined calcite particles in the gasifier at $t = 100$ s and $t = 30$ s, respectively. m and m_1 are the total number of calcined calcite particles in the combustor at $t = 100$ s and $t = 30$ s, respectively. $m_{\text{CaO } j, \, 100 \text{ s}}$ is the CaO mass in calcined calcite particle

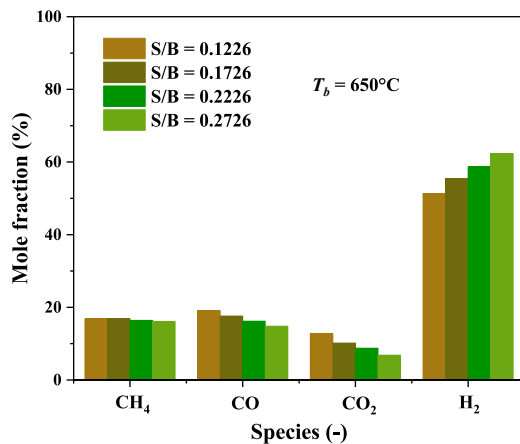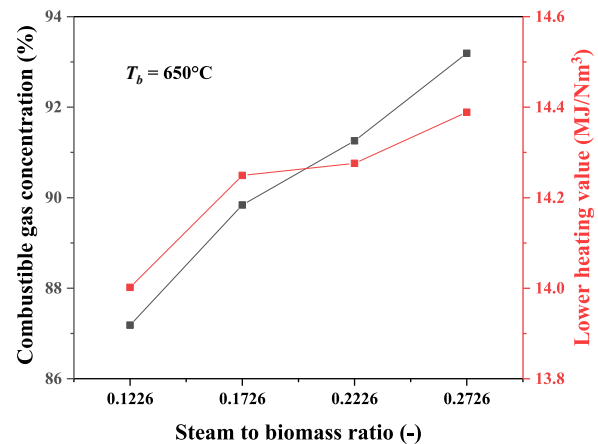(a)   (b)

Fig. 15. Variation of the CaO/$CaCO_3$ conversion with gasification temperature: (a) variation of CaO conversion with gasification temperature in the gasifier; (b) variation of $CaCO_3$ conversion with gasification temperature in the combustor.

(a)   (b)

Fig. 16. The concentration of gas species (a) and CGC and LHV (b) under the AER gasification condition as a function of the S/B ratio.
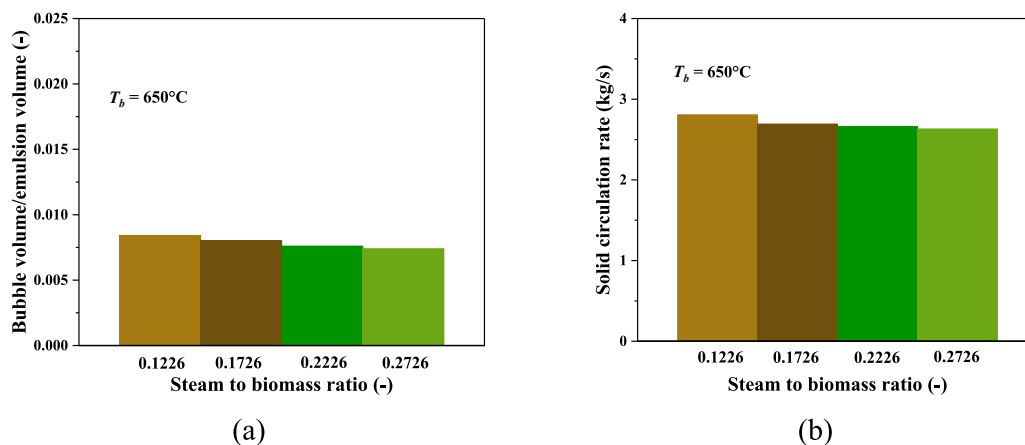
Fig. 17. The B/E ratio in the gasifier (a) and solid circulation rate between the two reactors (b) under the AER gasification condition as a function of the S/B ratio.
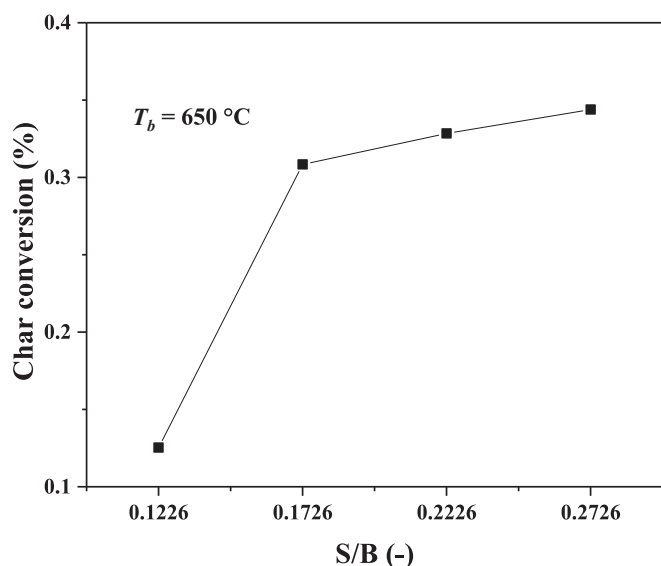

Fig. 18. Variation of the char conversion with the S/B ratio.

j in the gasifier at *t* = 100 s; $m_{CaO\,j,\,30\,s}$ is the CaO mass in calcined calcite particle *j* in the gasifier at *t* = 30 s. $m_{CaCO3\,k,\,100\,s}$ is the CaCO$_3$ mass in calcined calcite particle *k* in the combustor at *t* = 100 s, $m_{CaCO3\,k,\,30\,s}$ is the CaCO$_3$ mass in calcined calcite particle *k* in the combustor at *t* = 30 s. Fig. 15 shows the variation of the CaO/CaCO$_3$ conversion under

different gasification temperatures. A higher temperature promotes the carbonation reaction and increases the CaO conversion accordingly. The variation trend of the CaCO$_3$ conversion with gasification temperature is positively correlated with that of the CaO conversion. Higher temperature intensifies the conversion of CaO in the gasifier. The bed material particles with higher CaCO$_3$ content enter the combustor, which promotes the calcination reaction and strengthens the conversion of CaCO$_3$. Therefore, the CaCO$_3$ conversion increases with the increase in gasification temperature.

4.3.2. Steam-to-biomass ratio

Fig. 16 illustrates the effect of the S/B ratio on gasification performance under the AER gasification condition. To avoid the impact of the variation of inlet steam flow on the gas–solid flow motions within the reactor, different S/B ratios are achieved by varying the biomass feed rate but maintaining the inlet steam flow rate constant. As the S/B ratio rises, the H$_2$ concentration rises from 51.3% to 62.27%, whereas the CO$_2$ concentration decreases from 12.82% to 6.81%, the CH$_4$ concentration decreases from 16.84% to 16.12%, and the CO concentration decreases from 19.04% to 14.79%. A higher S/B ratio promotes methane steam reforming reaction (R8) and water–gas shift reaction (R2), thereby increasing the H$_2$ concentration but reducing the CO and CH$_4$ concentrations. At a low S/B ratio, more biomass particles are transported into the gasifier, resulting in the generation of a large amount of CO$_2$, which could not be fully removed by CaO. Therefore, the CO$_2$ concentration decreases as the S/B ratio increases. A higher S/B ratio increases the CGC from 87.18% to 93.19% and the LHV from 14.0 MJ/Nm^3 to 14.39 MJ/Nm^3. A higher S/B ratio improves AER gasification performance.
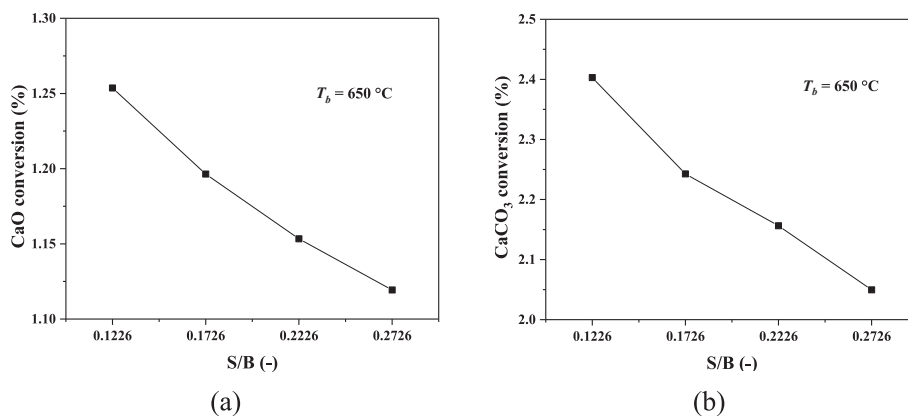

Fig. 19. Variation of the CaO/CaCO$_3$ conversion with the S/B ratio: (a) variation of CaO conversion with the S/B ratio in the gasifier; (b) variation of CaCO$_3$ conversion with the S/B ratio in the combustor.
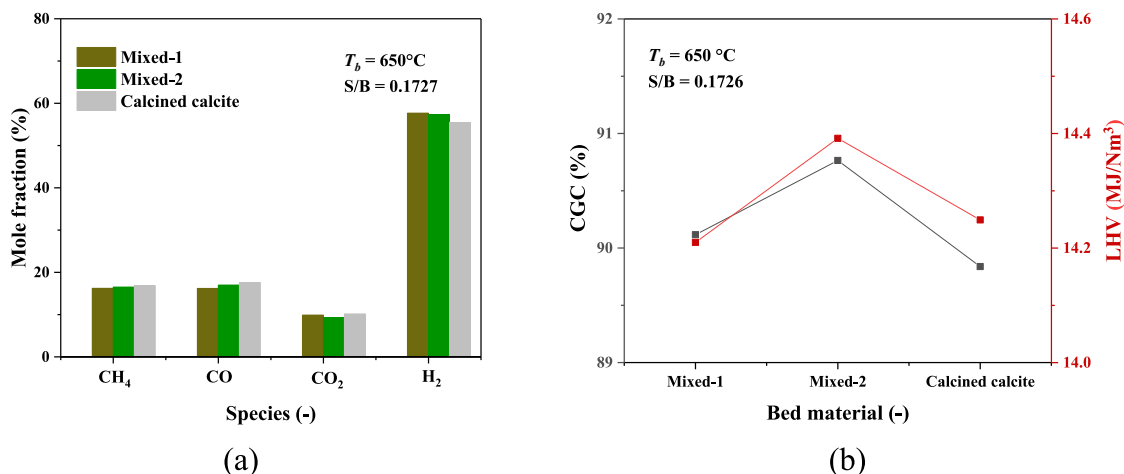
Fig. 20. The concentration of gas species (a) and CGC and LHV (b) under the AER gasification condition as a function of bed material.

Fig. 17 illustrates the effect of the S/B ratio on the B/E ratio and solid circulation rate between the two reactors under the AER gasification condition. At a low S/B ratio, more biomass particles are transported into the gasifier, and more gas is produced through pyrolysis and gasification processes. Therefore, the B/E ratio in the gasifier is larger at a low S/B ratio and leads to a larger particle mass flow rate between the reactors.

Fig. 18 shows the variation of the char conversion in the gasifier with the S/B ratio. Different S/B ratios are achieved by varying the biomass feed rate but maintaining the inlet steam flow rate constant. A higher S/B ratio promotes the char gasification reactions and thus leading to a higher char conversion. Therefore, the char conversion increases with the increase in the S/B ratio. Fig. 19 gives the variation of the CaO conversion in the gasifier and the $CaCO_3$ conversion in the combustor with the S/B ratio. With a lower S/B ratio, more biomass enters the gasifier, producing a large amount of CO_2, which promotes the carbonation reaction and a higher CaO conversion. Therefore, as the S/B ratio increases, the CaO conversion decreases. The variation trend of the $CaCO_3$ conversion with the S/B ratio is positively correlated with that of the CaO conversion. With a higher S/B ratio, bed material particles with lower $CaCO_3$ content enter the combustor, which inhibits the calcination reaction and weakens the conversion of $CaCO_3$, and the $CaCO_3$ conversion decreases as the S/B ratio increases.

4.3.3. Bed material

Fig. 20 shows the effect of bed material on gasification performance under the AER gasification condition. Three groups of bed material particles are set to investigate the effects of bed material on the AER gasification performance. The three groups of bed material particles are mixed-1, mixed-2, and calcined calcite, respectively, where the mixed-1 refers to the bed material with a ratio of olivine: calcined calcite = 1:1, mixed-2 refers to the bed material with a ratio of olivine: calcined calcite = 1:3. As shown in the figure, with the increase in the proportion of calcined calcite in bed material particles, the concentrations of CH_4 and CO increase, the concentration of H_2 decreases, and the concentration of CO_2 has a trend of first decreasing and then increasing. With the bed material with a low calcined calcite ratio (mixed-1), the solid circulation rate increases, and more heat is transported to the gasifier with the bed material particles as the carrier, which promotes the methane steam reforming reaction (R8) and water gas shift reaction (R9). Therefore, the bed material with a low calcined calcite ratio (mixed-1) promotes the decrease of CH_4 and CO concentrations and the increase of H_2 concentration. As the proportion of calcined calcite in the bed material increases (mixed-2), the solid circulation rate decreases and the heat transported to the gasifier decreases, leading to the weakening of the methane steam reforming reaction (R8) and water gas
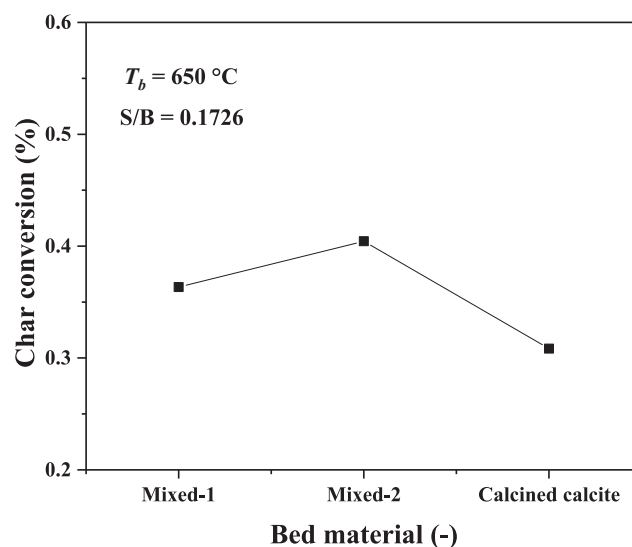

Fig. 21. Variation of the char conversion with bed material.

shift reaction (R9), and an increase of the concentrations of CH_4 and CO and a decrease of the concentration of H_2. As the proportion of calcined calcite in the bed material particles increases, more CO_2 is absorbed by CaO, and the CO_2 concentration decreases. With the bed material that is fully composed of calcined calcite, the solid circulation rate is further reduced compared with the mixed bed materials (mixed-1, mixed-2), and the heat transported to the gasifier is reduced, leading to the gasification reactions and carbonation reaction are weakened. Therefore, with the bed material that is fully composed of calcined calcite, the concentrations of CH_4, CO, and CO_2 increase, and the concentration of H_2 decreases. Fig. 20(b) shows the effects of bed material on the CGC and LHV. As the proportion of calcined calcite in the bed material increases, both LHV and CGC tend to increase first and then decrease. Therefore, in engineering practice, it can be considered to improve the gasification performance of AER by adjusting the bed material.

Fig. 21 shows the variation of the char conversion in the gasifier with bed material. As the proportion of calculated calcite increases, the char conversion increases first and then decreases. Compared with mixed-1, the increase in the proportion of calcined calcite in mixed-2 bed material promotes the carbonation reaction, which in turn affects its related parallel reactions (char gasification (R2), water–gas shift (R9), etc.), thereby strengthening the char conversion. With the bed material that is fully composed of calcined calcite, the larger particle size leads to a
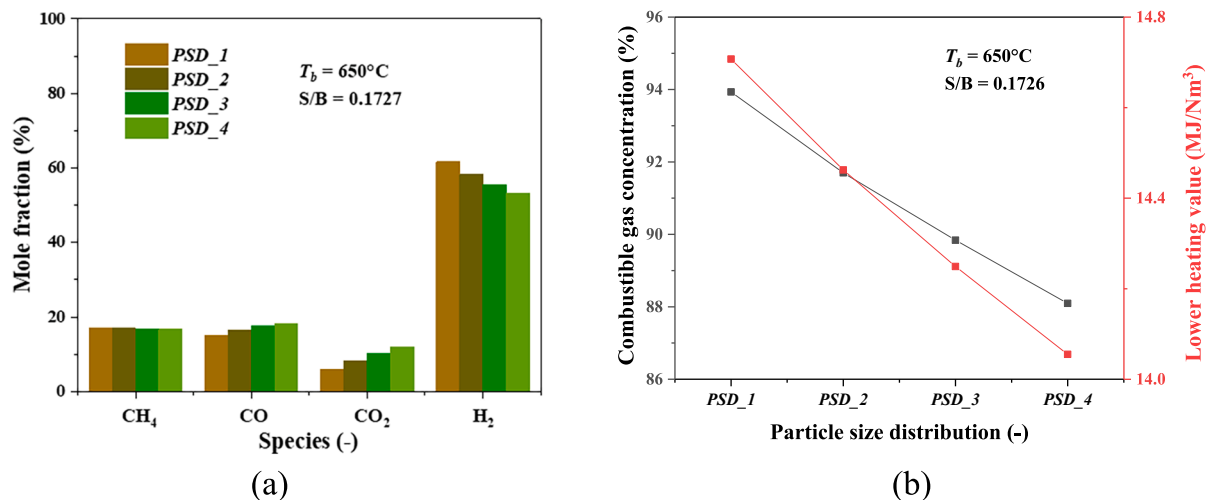
Fig. 22. The concentration of gas species (a) and CGC and LHV (b) under the AER gasification condition as a function of the PSD.
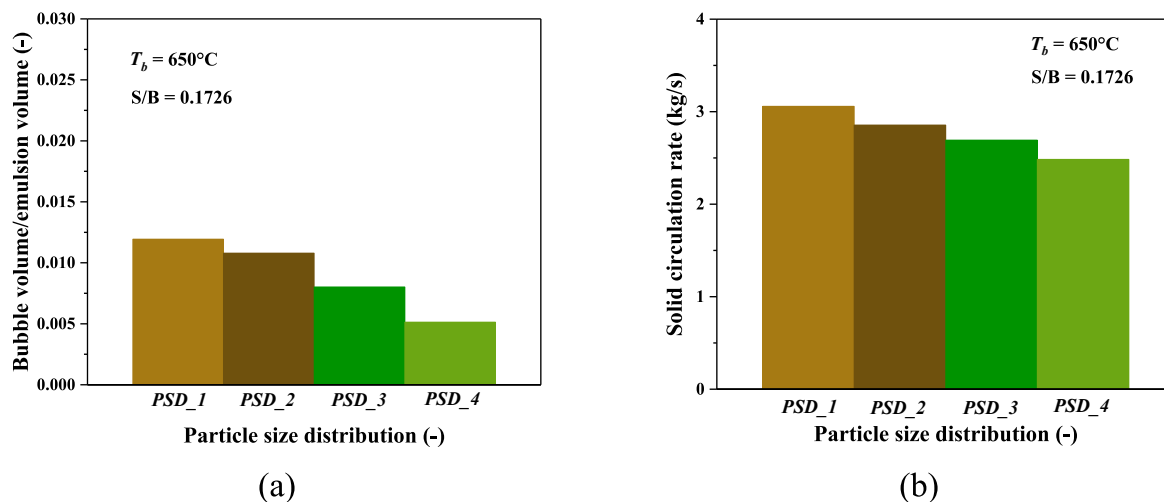

Fig. 23. The B/E ratio of gasifier (a) and solid circulation rate between the two reactors (b) under the AER gasification condition as a function of the PSD.

lower solid circulation rate, which further leads to a further decrease in the heat transported to the gasifier and the related gasification reactions are weakened, leading to the char conversion decreases.

4.3.4. Particle size distribution

Four groups of PSDs are set to investigate the effects of particle size on AER gasification performance. All the PSDs follow a normal distribution. The PSD of the four groups are as follows: 0.4 ~ 1.2 mm with an average diameter of 0.76 mm (*PSD_1*), 0.45 ~ 1.25 mm with an average diameter of 0.81 mm (*PSD_2*), 0.5 ~ 1.3 mm with an average diameter of 0.864 mm (*PSD_3*), 0.55 ~ 1.35 mm with an average diameter of 0.92 mm (*PSD_4*), respectively. Larger particle sizes should be used to reduce the particle circulation rate to maintain a lower temperature in the gasifier and maintain the progress of the carbonation reaction. Further increasing particle size leads to a significantly low particle circulation rate that provides insufficient heat for the reactions in the gasifier. In contrast, further decreasing particle size leads to a remarkably high solid circulation rate that rises the temperature in the gasifier, which inhibits the carbonation reaction and weakens the AER gasification performance. Therefore, narrow ranges of particle size distributions are adopted in this work to evaluate the effects of PSDs on the AER gasification performance. As shown in Fig. 22, with the increase of the particle size, the CO_2 concentration rises from 6.07% to 11.9%, the CO concentration rises from 15.17% to 18.23%, the H_2 concentration

decreases from 61.72% to 53.14%, and the CH_4 concentration decreases from 17.05% to 16.73%. The increase in CO_2 concentration makes CGC and LHV decrease with the increase in particle size. A smaller particle size enhances the AER gasification performance.

As shown in Fig. 23, the solid circulation rate between the reactors and the B/E ratio decreases with the increasing particle size. In the case of larger particle size, the bubble volume decreases, and the gas–solid motions in the gasifier tend to be gentle, leading to a lower solid circulation rate between the reactors and reduced gas–solid contact efficiency. The lower solid circulation rate weakens the heat transfer between the reactors and affects the progress of the reactions in the gasifier. In addition, the reduced gas–solid contact efficiency under the condition of larger particle size weakens the carbonation reaction and affects related parallel reactions, leading to higher CO_2 and CO concentrations and lower H_2 concentrations.

5. Conclusion

In this study, the AER gasification process in an 8 MW$_{th}$ DFB reactor is numerically studied by integrating the MP-PIC framework with complex reaction kinetics regarding gasification, carbonation, and calcination. After model validation and superiority demonstration by comparing with the conventional gasification, the effects of several key operating parameters on the AER gasification performance are studied.

The followings conclusions can be drawn:

1) The reaction kinetics considering carbonation and calcination are confirmed to be reasonable to describe the conventional and AER gasification processes. Compared with conventional gasification, AER gasification reduces CO_2 concentration by 55.8% but promotes H_2 concentration by 15.3%. For the conventional and AER gasification processes, the LHV of the gas products is 10.99 MJ/Nm^3 and 14.25 MJ/Nm^3, respectively, while the CGC is 77.02% and 89.84%, respectively, demonstrating the improvement of gas quality by the AER gasification technology.

2) The temperature in the gasifier and combustor under the AER gasification condition is lower than that under the conventional gasification condition, beneficial to the progress of the carbonation reaction and the improvement of the quality of the syngas. The bubble dynamics dominate the hydrodynamics in the gasifier. In the gasifier, biomass particles tend to distribute on the bed surface due to size-induced and density-induced segregation. The solid circulation rate between the reactors under the conventional gasification condition is one order of magnitude larger than that under the AER gasification condition. The lower particle mass flow rate under the AER gasification condition ensures the stable operation of the gasifier at a lower operating temperature.

3) Higher temperatures and higher S/B ratios improve the AER gasification performance. At high temperatures, the gas volume expands, and the B/E ratio increases, leading to more intense gas–solid motions in the gasifier, which enhances the particle transport between the reactors and maintains the temperature in the gasifier. Moreover, Higher temperature enhances the char conversion in the gasifier, the CaO conversion, and the $CaCO_3$ conversion in the combustor. A higher S/B ratio promotes the char conversion in the gasifier but harms the CaO conversion and the $CaCO_3$ conversion in the combustor.

4) The mixed bed material enhances the solid circulation rate and heat transfer between reactors, thus promoting the gasification reactions and carbonation reactions, leading to an improvement in gasification performance. In engineering practice, it can be considered to improve the gasification performance of AER by adjusting the bed material.

5) Smaller particle sizes improve the B/E ratio, intensify the gas–solid motions, strengthen the particle transport between the reactors, and improve the gas–solid contact efficiency in the gasifier. Accordingly, the carbonation reaction is enhanced, and CO_2 concentration is reduced. The promotion of the carbonation reaction drives parallel reactions to favor H_2 generation and CO reduction.

Declaration of Competing Interest

The authors declare that they have no known competing financial interests or personal relationships that could have appeared to influence the work reported in this paper.

Data availability

Data will be made available on request.

Acknowledgement

Supplementary data

Supplementary data to this article can be found online at https://doi.org/10.1016/j.cej.2023.142981.

References

[1] X.T. Li, J.R. Grace, C.J. Lim, A.P. Watkinson, H.P. Chen, J.R. Kim, Biomass gasification in a circulating fluidized bed, Biomass Bioenergy 26 (2004) 171–193.

[2] S. Li, S. Xu, S. Liu, C. Yang, Q. Lu, Fast pyrolysis of biomass in free-fall reactor for hydrogen-rich gas, Fuel Process. Technol. 85 (2004) 1201–1211.

[3] D. Kong, K. Luo, S. Wang, J. Yu, J. Fan, Particle behaviours of biomass gasification in a bubbling fluidized bed, Chem. Eng. J. 428 (2022), 131847.

[4] F. Saleem, J. Harris, K. Zhang, A. Harvey, Non-thermal plasma as a promising route for the removal of tar from the product gas of biomass gasification–a critical review, Chem. Eng. J. 382 (2020) 122761.

[5] L. Yan, C.J. Lim, G. Yue, B. He, J.R. Grace, Simulation of biomass-steam gasification in fluidized bed reactors: model setup, comparisons and preliminary predictions, Bioresource Technol. 221 (2016) 625–635.

[6] J.P. Ciferno, J.J. Marano, Benchmarking biomass gasification technologies for fuels, chemicals and hydrogen production, US Department of Energy, National Energy Technology Laboratory, 2002.

[7] R.B. Bates, A.F. Ghoniem, W.S. Jablonski, D.L. Carpenter, C. Altantzis, A. Garg, J. L. Barton, R. Chen, R.P. Field, Steam-air blown bubbling fluidized bed biomass gasification (BFBBG): multi-scale models and experimental validation, AIChE J 63 (2017) 1543–1565.

[8] J. Udomsirichakorn, P. Basu, P.A. Salam, B. Acharya, Effect of CaO on tar reforming to hydrogen-enriched gas with in-process CO2 capture in a bubbling fluidized bed biomass steam gasifier, Int. J. Hydrogen Energ. 38 (2013) 14495–14504.

[9] C.A. Jordan, G. Akay, Occurrence, composition and dew point of tars produced during gasification of fuel cane bagasse in a downdraft gasifier, Biomass Bioenergy 42 (2012) 51–58.

[10] D. Ross, R. Noda, M. Horio, A. Kosminski, P. Ashman, P. Mullinger, Axial gas profiles in a bubbling fluidised bed biomass gasifier, Fuel 86 (2007) 1417–1429.

[11] S. Chen, D. Wang, Z. Xue, X. Sun, W. Xiang, Calcium looping gasification for high-concentration hydrogen production with CO2 capture in a novel compact fluidized bed: simulation and operation requirements, Int. J. Hydrogen Energ. 36 (2011) 4887–4899.

[12] L. Han, Q. Wang, Y. Yang, C. Yu, M. Fang, Z. Luo, Hydrogen production via CaO sorption enhanced anaerobic gasification of sawdust in a bubbling fluidized bed, Int. J. Hydrogen Energ. 36 (2011) 4820–4829.

[13] S. Koppatz, C. Pfeifer, R. Rauch, H. Hofbauer, T. Marquard-Moellenstedt, M. Specht, H2 rich product gas by steam gasification of biomass with in situ CO2 absorption in a dual fluidized bed system of 8 MW fuel input, Fuel Process. Technol. 90 (2009) 914–921.

[14] N. Poboss, K. Swiecki, A. Charitos, C. Hawthorne, M. Zieba, G. Scheffknecht, Experimental investigation of the absorption enhanced reforming of biomass in a 20 kWth dual fluidized bed system, Int. J. Thermodyn. 15 (2012) 53–59.

[15] C. Pfeifer, B. Puchner, H. Hofbauer, In-situ CO2-absorption in a dual fluidized bed biomass steam gasifier to produce a hydrogen rich syngas, Int. J. Chem. React. Eng. 5 (2007).

[16] W. Yin, S. Wang, K. Zhang, Y. He, Numerical investigation of in situ gasification chemical looping combustion of biomass in a fluidized bed reactor, Renew. Energ. 151 (2020) 216–225.

[17] F. Alobaid, N. Almohammed, M. Massoudi Farid, J. May, P. Rößger, A. Richter, B. Epple, Progress in CFD simulations of fluidized beds for chemical and energy process engineering, Prog. Energ. Combust. 91 (2022) 100930.

[18] S. Wang, Y. Shen, Particle-scale study of heat and mass transfer in a bubbling fluidised bed, Chem. Eng. Sci. 240 (2021), 116655.

[19] T. Zhou, S. Yang, Y. Wei, J. Hu, H. Wang, Impact of wide particle size distribution on the gasification performance of biomass in a bubbling fluidized bed gasifier, Renew. Energ. 148 (2020) 534–547.

[20] R.K. Thapa, A. Frohner, G. Tondl, C. Pfeifer, B.M. Halvorsen, Circulating fluidized bed combustion reactor: computational particle fluid dynamic model validation and gas feed position optimization, Comput. Chem. Eng. 92 (2016) 180–188.

[21] Z. Wan, S. Yang, Y. Sun, Y. Wei, J. Hu, H. Wang, Distribution and particle-scale thermochemical property of biomass in the gasifier of a dual fluidized bed, Energ. Convers. Manage. 209 (2020) 112672.

[22] S. Kraft, F. Kirnbauer, H. Hofbauer, Influence of drag laws on pressure and bed material recirculation rate in a cold flow model of an 8MW dual fluidized bed system by means of CPFD, Particuology 36 (2018) 70–81.

[23] D.M. Snider, S.M. Clark, P.J. O'Rourke, Eulerian-Lagrangian method for three-dimensional thermal reacting flow with application to coal gasifiers, Chem. Eng. Sci. 66 (2011) 1285–1295.

[24] P.J.O. Rourke, D.M. Snider, An improved collision damping time for MP-PIC calculations of dense particle flows with applications to polydisperse sedimenting beds and colliding particle jets, Chem. Eng. Sci. 65 (2010) 6014–6028.

[25] J. Xu, L. Qiao, Mathematical modeling of coal gasification processes in a well-stirred reactor: effects of devolatilization and moisture content, Energ. Fuel. 26 (2012) 5759–5768.

[26] D. Kong, S. Wang, K. Luo, C. Hu, D. Li, J. Fan, Three-dimensional simulation of biomass gasification in a full-loop pilot-scale dual fluidized bed with complex geometric structure, Renew. Energ. 157 (2020) 466–481.

[27] H. Liu, R.J. Cattolica, R. Seiser, C. Liao, Three-dimensional full-loop simulation of a dual fluidized-bed biomass gasifier, Appl. Energ. 160 (2015) 489–501.

[28] C. Loha, H. Chattopadhyay, P.K. Chatterjee, Three dimensional kinetic modeling of fluidized bed biomass gasification, Chem. Eng. Sci. 109 (2014) 53–64.

[29] J. Yu, C. Yao, X. Zeng, S. Geng, L. Dong, Y. Wang, S. Gao, G. Xu, Biomass pyrolysis in a micro-fluidized bed reactor: characterization and kinetics, Chem. Eng. J. 168 (2011) 839–847.

[30] A. Tanksale, J.N. Beltramini, G.M. Lu, A review of catalytic hydrogen production processes from biomass, Renew. Sustain. Energy Rev. 14 (2010) 166–182.

[31] M. Balat, M. Balat, E. Kırtay, H. Balat, Main routes for the thermo-conversion of biomass into fuels and chemicals. Part 1: pyrolysis systems, Energ. Convers Manage 50 (2009) 3147–3157.

[32] J. Udomsirichakorn, P.A. Salam, Review of hydrogen-enriched gas production from steam gasification of biomass: the prospect of CaO-based chemical looping gasification, Renew. Sustain. Energy Rev. 30 (2014) 565–579.

[33] S. Kraft, F. Kirnbauer, H. Hofbauer, CPFD simulations of an industrial-sized dual fluidized bed steam gasification system of biomass with 8 MW fuel input, Appl. Energ. 190 (2017) 408–420.

[34] S. Sazhin, Modelling of heating, evaporation and ignition of fuel droplets: combined analytical, asymptotic and numerical analysis, J. Phys.: Conf. Ser., IOP Publ. (2005) 12.

[35] E.H. Baker, 87. The calcium oxide–carbon dioxide system in the pressure range 1–300 atmospheres, J. Chem. Soc. (Resumed) (1962) 464–470.

[36] P. Sun, J.R. Grace, C.J. Lim, E.J. Anthony, Determination of intrinsic rate constants of the CaO–CO2 reaction, Chem. Eng. Sci. 63 (2008) 47–56.

[37] Z. Li, N. Cai, Modeling of multiple cycles for sorption-enhanced steam methane reforming and sorbent regeneration in fixed bed reactor, Energ. Fuel. 21 (2007) 2909–2918.

[38] J.C. Schmid, U. Wolfesberger, S. Koppatz, C. Pfeifer, H. Hofbauer, Variation of feedstock in a dual fluidized bed steam gasifier—influence on product gas, tar content, and composition, Environ. Prog. Sustain. 31 (2012) 205–215.

[39] F. Kirnbauer, V. Wilk, H. Kitzler, S. Kern, H. Hofbauer, The positive effects of bed material coating on tar reduction in a dual fluidized bed gasifier, Fuel 95 (2012) 553–562.

[40] G. Soukup, C. Pfeifer, A. Kreuzeder, H. Hofbauer, In situ CO2 capture in a dual fluidized bed biomass steam gasifier–bed material and fuel variation, Chem. Eng. Technol.: Indus. Chem.-Plant Equipment-Process Eng.-Biotechnol. 32 (2009) 348–354.

[41] P. García-Ibanez, A. Cabanillas, J.M. Sánchez, Gasification of leached orujillo (olive oil waste) in a pilot plant circulating fluidised bed reactor, Preliminary results. Biomass Bioenergy 27 (2004) 183–194.

[42] S. Wang, K. Luo, C. Hu, L. Sun, J. Fan, Impact of operating parameters on biomass gasification in a fluidized bed reactor: an Eulerian-Lagrangian approach, Powder Technol. 333 (2018) 304–316.

[43] W. Yin, S. Wang, K. Zhang, Y. He, Investigation of oxygen-enriched biomass gasification with TFM-DEM hybrid model, Chem. Eng. Sci. 211 (2020), 115293.

[44] S. Wang, Y. Shen, CFD-DEM study of biomass gasification in a fluidized bed reactor: Effects of key operating parameters, Renew. Energ. 159 (2020) 1146–1164.

[45] S. Wang, K. Luo, J. Fan, CFD-DEM coupled with thermochemical sub-models for biomass gasification: Validation and sensitivity analysis, Chem. Eng. Sci. 217 (2020) 115550.

[46] S. Wang, Y. Shen, Coarse-grained CFD-DEM modelling of dense gas-solid reacting flow, Int. J. Heat Mass Transf. 184 (2022) 122302.